

The Mean Echo and Echo Cross Product From a Beamforming Interferometric Altimeter and Their Application to Elevation Measurement

D. J. Wingham, Laurent Phalippou, C. Mavrocordatos, and D. Wallis

Abstract—This paper describes the echo from a beamforming interferometric altimeter from a uniformly scattering surface inclined at an angle to a sphere, underlain by a uniformly scattering volume. The rough “surface” impulse response and the echo and interferometric cross product are determined as functions of the beam direction and the vector surface gradient. These expressions are used to determine the multilooked echo and interferometric phase from such a system. The “effective” number of looks and the multilooked echo coherence, which determine the statistics of the echo power and the interferometric phase, are defined. The dependence of the multilooked echo power and interferometric phase are investigated as functions of the surface vector gradient, surface roughness, volume scattering, and SNR. These behaviors are illustrated using values based on a practical system. The precision of the elevation measurement is examined in the light of the effective number of looks and the coherence of the multilooked echo and cross product. Some conclusions concerning the practical recovery of the range from the echo power are discussed.

Index Terms—CryoSat, ice sheets, interferometry, radar altimeter, sea ice.

I. INTRODUCTION

OVER THE PAST decade, new information concerning the shape, balance velocities, and contribution to sea level of the earth’s large ice sheets has been provided by satellite altimetry [1]–[4]. More recently, marine ice thickness has also been successfully recovered from satellite radar altimeter observations, providing the first observations of synoptic variations in Arctic sea ice mass [5], [6]. These new discoveries are the more remarkable for having employed opportunistically an altimeter design developed in the 1970s to determine the shape of the marine geoid from the normal-incidence backscatter from the ocean [7], a surface characterized by a very low curvature and homogeneous scattering properties. Nonetheless, the limitations of pulse-limited altimeter design have restricted the use of satellite altimeters in the determination of land and marine ice fluctuations. In the marginal regions of ice sheets where curvatures are significantly higher than in the interior, altimeter per-

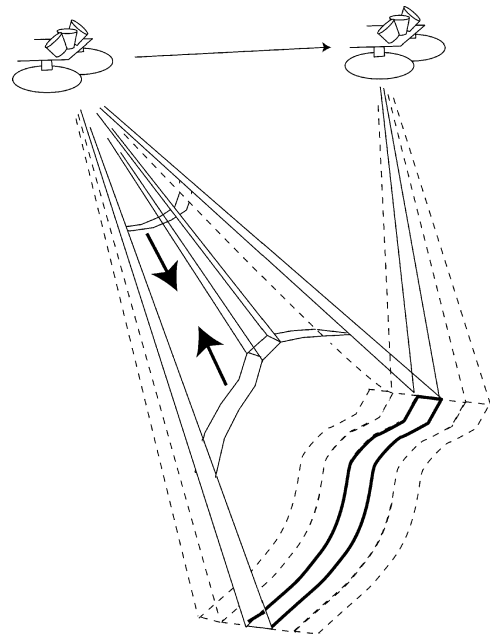


Fig. 1. Satellite altimeter concept. The directional gain of a normal-incidence pulse-limited altimeter determined by its antenna is narrowed in the along-track direction through the use of coherent processing. Following processing, the “effective” illumination of the surface is the product of the antenna gain and that of the “beam” formed by the processing; the net effect is that the altimeter effectively illuminates a narrow across-track strip (solid black line). A second antenna arranged in the across-track direction allows the across-track direction of the echo from the strip to be determined through interferometry. As the satellite moves along its orbit, more than one “look” at the same surface strip is possible, and statistical fluctuations of the echoes arising from the strip may be reduced through summation. In practice, multiple beams are formed at each satellite location (a few of these are indicated by dashed lines), and the multiple looks at a particular strip are formed by selecting a different beam from each satellite location.

formance is degraded or lost completely, while sea ice freeboard observations are presently limited to very large floes.

The limitations of pulse-limited altimeters, for the ice sheet problem at least, have led to the development of optical, laser altimeters, of which the first has recently been launched on the U.S. satellite “ICESat” [8]. On the other hand, the all-weather capability of radar sensors, and the thus far unique capability of the radar altimeter to measure sea ice freeboard, has led to selection of a beamforming interferometric radar altimeter as the main payload of the European “CryoSat” satellite [9], with a view to providing from mid-2004 observations of the earth’s ice sheets and Arctic sea ice. The concept of this instrument, which is illustrated in Fig. 1, is to employ beamforming in the along-track direction to improve on pulse-limited resolution and SNR, while, in regions of undulating terrain, to use across-track

Manuscript received August 1, 2003; revised May 26, 2004. This work was supported in part by the U.K. Natural Environment Research Council under Award F14/G6/95 and in part by the European Space Agency under Contract 12178/96/NL/SB.

D. J. Wingham and D. Wallis are with the Centre for Polar Observation and Modeling, University College London, London WC1E 6BT, U.K. (e-mail: djw@cpom.ucl.ac.uk; dww@cpom.ucl.ac.uk).

L. Phalippou is with Alcatel Space, 31037 Toulouse Cedex 1, France (e-mail: Laurent.phalippou@space.alcatel.fr).

C. Mavrocordatos is with the CryoSat Project, Earth Observation Programmes Development, European Space Agency, 2200 AG Noordwijk, The Netherlands (e-mail: Constantin.Mavrocordatos@esa.int).

Digital Object Identifier 10.1109/TGRS.2004.834352

interferometry to determine the across-track source of the scattered energy.

The instrument concept is not a new one. Conceptual combinations of synthetic aperture and interferometric radars for high-resolution altimetry were widely discussed in the late 1980s and early 1990s (e.g., see [10]), largely motivated by the then poor state of digital elevation models of the earth [11]. That problem was later solved by sideways-looking synthetic aperture radar (SAR) interferometry [12], but for the ice sheet mass imbalance problem in particular, the demand for precise elevation change resulted in the retention of a normal-incidence configuration, and more refined concept studies in the mid-1990s, guided to a degree by the heritage of existing pulse-limited hardware. Raney [13] described in some detail the along-track processing and resulting echo behavior of such a system, and Jensen [14] provided the basic equations for the recovery of the across-track location of the surface through the addition of interferometry. Phalippou *et al.* [15] reported on a numerical simulation of the performance of a combined system over land and marine ice surfaces. An aircraft “proof-of-concept” version has verified the assumptions of these system studies (<http://fermi.jhuapl.edu/d2p>). A detailed description of the actual CryoSat radar has been given in [16].

Raney and Jensen [13], [14] treat idealized cases in which the effective illumination (i.e., that resulting from the product of the antenna and beam directional gains) is described by a line that is normal to the along-track surface gradient. The purpose of this paper is to extend those treatments to include many of the factors bearing on the detailed shape and phase of the echo in the practical situation. It describes the mean properties of the echoes received by an interferometric beamforming altimeter operating above uniformly rough surface, inclined to a sphere, and underlain by a uniform scattering volume. It includes a description of the effect on the echo of the surface curvature and (vector) gradient, the directional profile of the antenna and beam gains, the beam look direction, the multilooking of the beams, the transmitted pulse shape, the surface roughness, the volume scattering, and the thermal noise, and it keeps the treatment analytic to the extent that the parameters of the practical system permit.

The form of this paper is as follows. In Section II, approximate analytic expressions in a satellite-fixed reference frame are developed for the mean echo and echo cross product. The approach is based on the use of the Fresnel approximation whose application to satellite pulse-limited geometries was justified in detail in [17]. Once allowance is made for the gain of the beam, however, it is not possible in the general case to give a closed form for the impulse response, save the normal-incidence special case and the asymptotic behavior at the limits of large delay times. In Section III, the “slant-range correction” (termed “delay-compensation” by Raney) that is used to align the echoes prior to multilooking is described, and the power and phase of single-look echoes as functions of surface geometry are described. In Section IV, the multilooked echoes, and appropriate measures of the “effective” number of looks and multilooked coherence are introduced, and their properties described. Section V describes how the multilooked echoes vary with surface roughness, volume scattering and SNR.

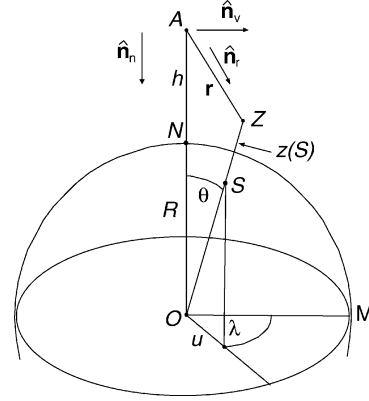


Fig. 2. Center of the interferometer baseline A is located at an altitude h above the sphere of radius R . In detail, we allow the scattering surface to differ slightly from that of the sphere by a normal elevation $z(S)$. For clarity, this elevation is shown exaggerated in the figure; it is assumed, however, that $z(S)$ is small enough that the direction from A of a scattering element at Z , \hat{n}_r , is equal to that of the point S . A point S on the sphere is described by a polar angle θ and an azimuthal angle λ . The axis of the polar angle is the line OA joining the origin of the sphere and the altimeter. The nadir point N lies at the intersection of OA and the sphere, and its direction when viewed from the altimeter is described by the unit vector \hat{n}_v . The origin of the azimuthal angle is the line OM in the equatorial plane that is coplanar with the unit vector \hat{n}_v in the direction of motion. It is assumed in this paper that \hat{n}_v and \hat{n}_n are orthogonal.

In Section VI, we discuss how the more realistic description of this paper effects the range and phase precision of the altimeter, and also identify limitations in our treatment of the instrument and the surface and volume scattering. The paper is concluded in Section VII with some remarks concerning the implications of the results for the detailed determination of the range from the echo power. Appendix A contains a list of symbols and the values used in the numerical illustrations. Appendix B describes some background to the statistics of the multilooked echo.

II. APPROXIMATE FORMS FOR THE ECHO POWER AND INTERFEROMETRIC CROSS PRODUCT

The geometrical arrangement considered in this paper is described in two figures: Fig. 2 shows the relation of the interferometer to the scattering surface and volume, and Fig. 3 the detailed arrangement of the interferometer itself.

We suppose that one antenna, labeled (1) and taken for definiteness to be that to the left of the flight direction, transmits a brief sequence of pulses whose field is $p_t^{1/2}(t)e^{i\omega_o t}$, where t is time, ω_o is the carrier radian frequency, p_t is the (compressed) power envelope, taken here to be

$$p_t(t) = \frac{p_0}{\sqrt{\pi}} \exp \left[-\left(\frac{t}{\tau_p} \right)^2 \right]. \quad (1)$$

τ_p is the altimeter delay resolution. With this definition, the total energy of the pulse is $p_0\tau_p$. The particular form of (1) is chosen for simplicity.

After some delay, both antennas receive a corresponding sequence of echoes scattered from the surface and volume. This sequence of echoes is coherently processed to narrow the sensitivity in the along-track direction around a particular angle to the nadir direction, which we term the “look angle,” resulting in

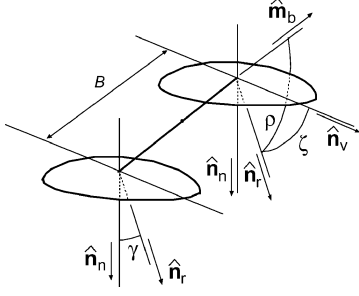


Fig. 3. Altimeter consists of two identical antennas whose one-way power gain g is a function only of the polar angle γ between the boresight direction, taken here to equal the nadir direction \hat{n}_n , and the direction of a scattering element \hat{n}_r . This gain is multiplied in the along-track direction by a “beam” whose one-way power gain d is a function of the angle ζ between the velocity vector \hat{n}_v and the direction of a scatterer \hat{n}_r . The antennas’ phase centers are separated by a baseline B whose direction is described by a unit vector \hat{m}_b , and the interferometer formed from the combination is sensitive only to the angle ρ between \hat{m}_b and \hat{n}_r .

the echoes $\Phi^{(1)}$ and $\Phi^{(2)}$ from each antenna. These echoes may be regarded as those formed from a system with a total directional gain that is the product of that of the antenna and that of a “beam” whose gain is concentrated around the look angle in the along-track direction.

In practice, the processing of each sequence is performed so as to simultaneously narrow the along-track gain, i.e., form beams, in a sequence of look directions distributed around the nadir direction. The sequence of echoes emerging from the consecutive beams may be regarded as those arising from consecutively illuminated strips of the surface, as illustrated in Fig. 1, and the processing may be arranged so that each echo appears to have arisen from the same, fixed location of the satellite. However, this paper is only concerned with the echo resulting from a particular strip (the solid lined strip in Fig. 1). In this case, one need only account explicitly for the echo corresponding to a single beam (i.e., look direction) from each satellite location, and this is the approach taken here.

This paper is concerned with mean values of cross products of the echoes $\Phi^{(1)}$ and $\Phi^{(2)}$, specifically the mean echo powers

$$p_r^{(1)} = E \left\{ \Phi^{(1)} \overline{\Phi^{(1)}} \right\} \quad p_r^{(2)} = E \left\{ \Phi^{(2)} \overline{\Phi^{(2)}} \right\} \quad (2)$$

and the mean cross product

$$\Psi^{(1,2)} = E \left\{ \Phi^{(1)} \overline{\Phi^{(2)}} \right\}. \quad (3)$$

In (2) and (3), the expectation $E\{\cdot\}$ denotes an average across an ensemble of scattering elements, and \overline{x} denotes the complex conjugate of x . The paper is also concerned with quantities derived from the echoes $\Phi^{(1)}$ and $\Phi^{(2)}$ by processes such as slant range correction (Section III) and multilooking (Section IV). We use the generic term “echo” to describe all of these quantities, but distinguish a particular echo by its notation and where needed by qualification (e.g., “multilooked echo”).

A. Approximations to the Scattering and Geometry

An exact description of the cross products requires a complete description of the geometry and of the random scattering

mechanisms. However, such a treatment is lengthy and unnecessary to the purpose of this paper. Here we limit ourselves to approximate forms that, first, are suitable for pulse-limited altimeter geometry in a low earth orbit, and, second, arise from treating the scattering as if it were due to small independent scatterers. The geometric approximations suitable for low-earth orbit, pulse-limited altimetry rest, essentially, on the smallness of the angles illuminated by the antennas, and on restricting the fluctuations of the surface about the sphere. A detailed justification for these approximations is given in [17]. In the present paper the approximations are simply identified, together with the additional modifications needed to describe the along-track beam.

We assume the antennas’ gain is axisymmetric about their boresight direction, taken to be the nadir direction \hat{n}_n , and given by the function

$$g(\cos \gamma) = g \left(\sqrt{1 - \sin^2 \gamma} \right) \equiv G e^{-\sin^2 \gamma / \gamma_a^2} \quad (4)$$

where γ is the angle between the nadir direction and that of a scattering element \hat{n}_r (Fig. 3). We assume in particular that

$$\gamma_a \ll 1 \quad (5)$$

which limits scattering elements of interest to those for which $\gamma \ll 1$, i.e., those in the vicinity of the point N (Fig. 2).

We allow that in detail the scattering surface differs slightly from the sphere itself by a normal elevation $z(S)$ (Fig. 2), but this elevation is assumed small enough that \hat{n}_r may be taken to be the direction of the point S on the sphere rather than the point Z . The smallness of γ then allows a simple approximation for angles and directions viewed from the satellite in terms of the spherical coordinates θ and λ of the point S . For this purpose, we imagine a second plane parallel to the equatorial plane of the sphere and passing through A with a polar axis in the direction of \hat{n}_n (see Fig. 2). The direction \hat{n}_r of any scattering element is then described by the polar angle γ and an azimuthal angle β . The approximation is then to take the azimuthal angle β of any scattering point to equal the azimuthal angle λ of the point S . In addition, the smallness of γ_a allows the approximation

$$\sin \gamma \sim \frac{R}{h} \sin \theta \quad (6)$$

for any scattering element of interest. Here, h is the radar altitude, and R is the radius of the sphere (Fig. 2).

We also assume that γ and z are small enough to allow the Fresnel approximation for the distance $|\mathbf{r}|$ between the points A and Z (Fig. 2), namely that

$$|\mathbf{r}| \sim h - z + \frac{R^2 \kappa}{2h} \sin^2 \theta \quad (7)$$

where we have also used (6). Here

$$\kappa = 1 + \frac{h}{R} \quad (8)$$

is a geometric factor that describes the departure of the spherical reference surface from that of a plane.

In this paper, we further restrict interest to surfaces with the specific form

$$z(\theta, \lambda) = R \sin \theta \tan \theta_p \cos(\lambda - \lambda_p). \quad (9)$$

This describes a surface that in the vicinity of the nadir point N (Fig. 2) maintains a gradient with respect to the sphere of $\tan \theta_p$ in the direction λ_p . This gradient is assumed small, so that an area element of the sphere may replace that of the scattering surface. It will become useful to identify that with this surface and the approximations of (6) and (7), the minimum distance between the point A and the surface occurs at a point on the sphere given by

$$\sin \theta = \frac{h}{R\kappa} \tan \theta_p \quad \lambda = \lambda_p \quad (10)$$

and that the minimum distance is

$$r_m = h - \frac{h}{2\kappa} \tan^2 \theta_p. \quad (11)$$

Turning next to the power gain d of the beam, we assume the processor is designed such that within the along-track plane (i.e., the plane defined by the vectors \hat{n}_v and \hat{n}_n) the maximum gain of the beam is in a direction making a polar angle ξ_b with the nadir direction \hat{n}_n . ξ_b is the look angle of the beam, where a positive value of ξ_b indicates the direction $\lambda = 0$. We further assume that unfocussed aperture synthesis is used, in which case this gain is solely a function of $\cos \zeta - \sin \xi_b$, where ζ is the angle between \hat{n}_v and \hat{n}_r (Fig. 3). We assume the form

$$d(\cos \zeta) = D_0 \exp \left[-\frac{1}{\zeta_b^2} (\cos \zeta - \sin \xi_b)^2 \right] \quad (12)$$

for the functional form of the gain. The angle ζ_b determines the angular width of the beam. We then again use (6) to approximate

$$\cos \zeta \sim \frac{R}{h} \sin \theta \cos \lambda \quad (13)$$

in the argument of this function.

In practice, the beam gain will depend on the aperture weighting used in processing the sequence of received echoes, and will generally be a periodic function. Equation (12), which ignores the periodicity of the beam, is chosen because it permits in at least one case an analytic result for the power impulse response (Section II-B). Separately, a practical processor will also need to vary to an extent the beam look angle to ensure the strips of Fig. 1 coincide as the satellite moves on its orbit. Because of this we only consider the case in which \hat{n}_v and \hat{n}_n are orthogonal: while this is not usually exactly the case in practice, the lack of orthogonality may be accounted for in the choice of ξ_b by the processor.

The next set of approximations concerns the nature of the ensemble of the scattering elements. We assume that these are small, that their individual phases are uniformly distributed on $[0, 2\pi]$ and that they are independent one from another. This means in particular that in the ensemble average cross product, only the phase difference at each antenna from individual scattering elements need be considered (and not those between

different elements). We assume that the baseline is small enough that the Fraunhofer approximation may be made for this phase difference, so that the complex element of the cross product from any scattering element takes the form $\exp[ikB \cos \rho]$, where ρ is the angle between the baseline vector \hat{m}_b and the direction \hat{n}_r of the scattering element (see Fig. 3), $k (= \omega_0/c)$ is the carrier wavenumber, and B is the interferometer baseline length. This is the one-way phase difference because the difference in path length only accrues of the return path.

The baseline vector \hat{m}_b is described by a polar angles ξ_i measured from \hat{n}_n and an azimuthal angle β_i measured from \hat{n}_v . The basic concept (Fig. 1) is to arrange that the baseline vector \hat{m}_b is orthogonal to \hat{n}_v and to \hat{n}_n , in which case $\xi_i = \pi/2$ and $\beta_i = \pi/2$, but we allow that β_i may not equal $\pi/2$ and that the polar angle ξ_i may depart by a small angle $\delta_i = \xi_i - \pi/2$ from this situation. In this case

$$\begin{aligned} \cos \rho &= \cos \xi_i \cos \xi + \sin \xi_i \sin \xi \cos(\beta_i - \beta) \\ &\sim \frac{R}{h} \sin \theta \cos(\beta_i - \lambda) - \sin \delta_i \end{aligned} \quad (14)$$

using again (6). (The departure of β_i from $\pi/2$ and δ_i are respectively the yaw and roll angles of the interferometer. In the examples in this paper we shall assume that these are zero, but it may be useful in the future to have included these here for completeness.) We also assume that the phase difference is the only difference between the echo at each antenna from a scattering element. Implicitly, this means we are assuming the travel time associated with the range differences is small in comparison with the duration of the transmitted pulse $p_t(t)$.

Turning to the mean scattering properties, we assume that the mean scattering surface geometry is described by a probability density function $s(z)$. In this paper, we suppose the roughness is the Gaussian distribution function

$$s(z) = \frac{1}{\sqrt{2\pi}\sigma_s} \exp \left[-\frac{z^2}{2\sigma_s^2} \right]. \quad (15)$$

The standard deviation of the surface roughness is then σ_s .

We also assume that the smallness of γ allows the assumption that only the two-way vertical path within the volume need be considered, and in this case the total scattering cross-section per unit volume may be described by a distribution function of depth $v(z)$, that is here taken to be

$$v(z) = \begin{cases} 0, & z < 0 \\ \frac{1}{2\pi c} \left(\sigma^0 \delta \left(\frac{2z}{c} \right) + \sigma_v^0 \alpha_v \exp \left(-\alpha_v \left(\frac{2z}{c} \right) \right) \right), & z \geq 0. \end{cases} \quad (16)$$

Here, σ^0 is the surface backscattering coefficient. σ_v^0 is defined such that $\sigma^0 + \sigma_v^0$ is the total scattering cross-section per unit area of the surface, and α_v is a parameter describing the total two-way attenuation within the volume. These are the parameters directly observable in the echo. In terms of more physical parameters, if σ_v is the backscatter coefficient per unit volume, c_v the electromagnetic wavespeed in the volume, k_t the transmission coefficient at the interface, and k_e the two-way extinction coefficient within the volume, then $\sigma_v^0 = \sigma_v k_t^2 / (2k_e)$ and $\alpha_v = c_v k_e$. See [17] for a more detailed discussion of the geometric assumptions that lead to (16). The explicit form for v of (16) was introduced by Arthern and Wingham [18].

B. Impulse Response, Echo Power, and Cross Product

With these approximations, the ensemble power and cross product may be expressed in terms of integrals over the spherical surface in the following form

$$\left\{ \begin{array}{l} p_r^{(1)}(t) \\ \Psi_{(1,2)}^{(1,2)}(t) \end{array} \right\} = \frac{c^2}{4} p_t(t) * s\left(\frac{ct}{2}\right) * v\left(\frac{ct}{2}\right) * \left\{ \begin{array}{l} \chi(t, 0) \\ \chi(t, B) \end{array} \right\} + \left\{ \begin{array}{l} p_n \\ 0 \end{array} \right\} \quad (17)$$

Here, p_n is the noise power, whose definition will be discussed more fully below. The function χ is the “impulse response”

$$\begin{aligned} \chi(t, B) = & \frac{\lambda^2 R^2}{16\pi^2 h^4} \int \int_{\text{Sphere}} \sin \theta d\theta d\lambda g^2(\cos \gamma) d(\cos \zeta) \\ & \cdot \exp[-ikB \cos \rho] \delta \\ & \cdot \left(t - \frac{2}{c} \left(h + \frac{R^2 \kappa}{2h} \right. \right. \\ & \left. \left. \sin^2 \theta - R \sin \theta \tan \theta_p \cos(\lambda - \lambda_p) \right) \right). \end{aligned} \quad (18)$$

In this expression, t is the travel time of the echo from the instant of transmission.

The impulse response may be reduced to a single integral by a change of variable that simplifies the argument of the δ -function. This may be done in a single step, but it is easier to appreciate its geometric significance if it is accomplished in three steps. If, first, one makes the variable change $u = R \sin \theta$, the integral is changed to one over a plane, which may be taken to be the equatorial plane of the sphere, and in which u is the radial coordinate (see Fig. 2). The approximation

$$R^2 \sin \theta d\theta = \frac{u du}{\left(1 - \left(\frac{u}{R}\right)^2\right)^{1/2}} \sim u du \quad (19)$$

is possible because the smallness of γ implies that only values of u for which $u/R \ll 1$ contribute significantly to the integral. In this coordinate system, the argument of the δ -function becomes

$$t - \frac{2h}{c} - \frac{\kappa}{ch} (u^2 - 2u u_m \cos(\lambda - \lambda_p))$$

where

$$u_m = \frac{h}{\kappa} \tan \theta_p \quad (20)$$

which is the radial coordinate in the equatorial plane of the vertical projection of the point on the surface whose distance to the altimeter is the minimum distance r_m defined by (20).

One may then determine that the argument of the δ -function is always negative for times $t < 2r_m/c$, while, for fixed times greater than this, setting the argument to zero describes a circle in the plane, centered at (u_m, λ_p) , with a radius equal to $\sqrt{(ch/\kappa)(t - 2r_m/c)}$. Thus, the projection of a line of constant range is a circle. By considering in a similar way the argument of the antenna gain one finds that the projection of a line of constant gain also a circle, this time centered at the origin O in the equatorial plane. Finally, one finds that the projection of a line of constant beam sensitivity is a straight line orthogonal to OM in Fig. 2. The line of maximum sensitivity crosses the line OM a distance $h \sin \xi_b$ from O . These findings are a consequence of

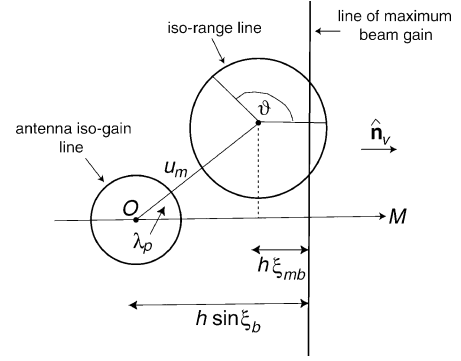


Fig. 4. Lines of constant range, antenna gain, and beam gain in the (u, λ) -plane.

the simplifications we have made to the actual geometry; they are illustrated in Fig. 4.

To reduce the integrals to a line integral around an isorange circle, one introduces new radial and azimuthal variables that transform the origin of the integral to the origin (u_m, λ_p) of the circle. The integral over the radial coordinate may then be done using the properties of the δ -function, leaving a single integral over the new azimuthal coordinate that we denote ϑ (see Fig. 4). The result is

$$\chi\left(\tau + \frac{2r_m}{c}, B\right) = 0 \quad \tau < 0 \quad (21)$$

while for $\tau \geq 0$

$$\begin{aligned} \chi\left(\tau + \frac{2r_m}{c}, B\right) = & \frac{\lambda^2 G^2 D_0 c}{32\pi^2 h^3 \kappa} e^{-(2/\gamma_a^2)((u_m^2/h^2) + (c\tau/h\kappa))} \\ & \cdot \exp\left[-ikB \left(\frac{u_m}{h} \cos(\lambda_p - \zeta_i) - \sin \delta_i\right)\right] \\ & \cdot \int_0^{2\pi} d\vartheta \exp\left(\frac{-4u_m}{\gamma_a^2 h} \sqrt{\frac{\tau c}{h\kappa}} \cos(\vartheta - \lambda_p)\right) \\ & \cdot \exp\left[-\frac{1}{\zeta_b^2} \left(\sqrt{\frac{\tau c}{h\kappa}} \cos \vartheta - \xi_{mb}\right)^2\right] \\ & \cdot \exp\left[-ikB \sqrt{\frac{\tau c}{h\kappa}} \cos(\vartheta - \zeta_i)\right]. \end{aligned} \quad (22)$$

Here τ is the echo delay relative to the time delay of the “first arrival” $2r_m/c$. The angle ξ_{mb} is given by

$$\xi_{mb} = \frac{1}{h} (h \sin \xi_b - u_m \cos \lambda_p). \quad (23)$$

The geometric interpretation of this angle is illustrated in Fig. 4. It is the angle between the normal to the along-track gradient and the direction of the maximum gain of the beam.

In general, (22) appears to be as far as one may take the calculation analytically. The difficulty is the term associated with the beam [the fourth line of (22)]. This term seems very resistant to an accurate approximation that holds for all τ at any particular value of ξ_{mb} . Asymptotic forms for large and small τ may be obtained, but we will not pursue these here.

One special case for which the power impulse response may be integrated occurs when $u_m = 0$, which describes a scattering surface coincident with the sphere, and $\xi_{mb} = 0$, which generally describes a situation in which the line of maximum sensitivity passes through the point of closest approach, and which,

with $u_m = 0$, describes the beam directed at the nadir point N in Fig. 2. In this case, and putting $\delta_i = 0$ for convenience, (22) becomes

$$\begin{aligned} \chi\left(\tau + \frac{2r_m}{c}, 0\right) \Big|_{\substack{u_m=0 \\ \xi_{mb}=0}} &= \frac{\lambda^2 G^2 D_0 c}{32\pi^2 h^3 \kappa} e^{-(2/\gamma_a^2)(c\tau/h\kappa)} \\ &\cdot \int_0^{2\pi} d\vartheta \exp\left[-\frac{1}{\zeta_b^2} \left(\sqrt{\frac{\tau c}{h\kappa}} \cos\vartheta\right)^2\right] \\ &= \frac{\lambda^2 G^2 D_0 c}{16\pi h^3 \kappa} e^{-(c\tau/h\kappa)((2/\gamma_a^2)+(1/2\zeta_b^2))} \\ &\cdot I_0\left(\frac{c\tau}{2h\kappa\zeta_b^2}\right). \end{aligned} \quad (24)$$

Here, I_0 is the modified Bessel function. The asymptotic behavior of this function provide the limiting behaviors

$$\begin{aligned} \chi\left(\tau + \frac{2r_m}{c}, 0\right) \Big|_{\substack{u_m=0 \\ \xi_{mb}=0}} &\sim \frac{\lambda^2 G^2 D_0 c}{16\pi h^3 \kappa} \tau \rightarrow 0^+ \\ &\sim \frac{\lambda^2 G^2 D_0 \zeta_b}{16\pi^{3/2} h^{5/2}} e^{-(2/\gamma_a^2)(c\tau/h\kappa)} \sqrt{\frac{\kappa c}{\tau}} \tau \rightarrow \infty. \end{aligned} \quad (25)$$

For small delays, the impulse response has the h^{-3} dependence that is characteristic of pulse-limited altimetry. This arises because, for small delays, the isorange line (“range-ring”) falls entirely within the beam gain. At longer delays, the dependence changes to $h^{-5/2}$. At these delays, the beam gain illuminates only a small part of the range ring (rather as drawn in Fig. 4), and the system is beamlimited along-track, while remaining pulse-limited across track.

Taking the limit $\zeta_b \rightarrow 0$ in (25) whilst insisting $D_0 \zeta_b$ remains finite has the effect of making the beam gain negligible except along the line of scatterers that coincide with the maximum gain of the beam, and in this case the large τ limit of (25) holds for all $\tau > 0$, as observed previously [13], [19].

A second special case occurs on setting the beam gain to unity. In this case, (22) for the power impulse response reduces to that of a conventional, pulse-limited altimeter. In fact, in this case

$$\begin{aligned} \chi\left(\tau + \frac{2r_m}{c}, 0\right) &= \frac{\lambda^2 G^2 c}{32\pi^2 h^3 \kappa} e^{-(2/\gamma_a^2)((u_m^2/h^2)+(c\tau/h\kappa))} \\ &\cdot \int_0^{2\pi} d\vartheta \exp\left(-\frac{4u_m}{\gamma_a^2 h} \sqrt{\frac{\tau c}{h\kappa}} \cos(\vartheta - \lambda_p)\right) \\ &= \frac{\lambda^2 G^2 c}{16\pi h^3 \kappa} e^{-(2/\gamma_a^2)((u_m^2/h^2)+(c\tau/h\kappa))} \\ &\cdot I_0\left(\frac{4u_m}{\gamma_a^2 h} \sqrt{\frac{\tau c}{h\kappa}}\right) \end{aligned} \quad (26)$$

which is Brown’s rough surface impulse response [20], once allowance is made for the fact that Brown considered a “mispointed” antenna, whereas we consider a surface inclined to a sphere.

Expressing the impulse response in terms of the delay τ is conventional in pulse-limited altimetry. In the case of the beam-forming altimeter this is not the most useful representation. Given that the along-track beam width ζ_b is very much smaller

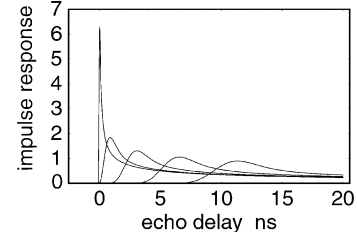


Fig. 5. Normalized power impulse response $32\pi^2 h^3 \kappa \chi_p / (\lambda^2 G^2 D_0 c)$ of a spherical surface for the sequence of values of look angle $\xi_b = (0, 0.5, 1.0, 1.5, 2.0) \cdot 10^{-3}$ rad. Increasing look angle corresponds to a smaller maximum.

than that of the antenna γ_a , the integral in (22) is dominated by the contribution of the beam. One may anticipate from (22) that the “earliest appreciable part” of the echo occurs around the earliest times for which the argument of the beam function in (22) is zero, i.e., when

$$\tau = \frac{h\kappa}{c} \xi_{mb}^2. \quad (27)$$

This is illustrated in Fig. 5, which shows a set of five, normalized impulse responses from a spherical surface calculated for the look angles $\xi_b = (0, 0.5, 1.0, 1.5, 2.0) \cdot 10^{-3}$ rad. In this case $\xi_b = \xi_{mb}$, so the figure simultaneously illustrates the same sequence of values of ξ_{mb} . The rightward shift in the maximum of the impulse response, increasing parabolically with ξ_{mb} , is apparent in the figure. [The most leftward of the impulses responses is that of (24); the remainder were calculated numerically from (22).]

One other effect of increasing ξ_{mb} is also worth noting: the fall in magnitude and broadening of the impulse responses. This is due to the fact that as ξ_{mb} increases, the range of delay times occupied by the fixed angular width of the beam also increases, quadratically with ξ_{mb} . There is also a drop in magnitude as ξ_{mb} increases due to the change of the antenna gain with delay time [the leading exponential in (22)], but, in fact, for the range of τ in this example, the change of antenna gain is very small, and the illustrated effect is almost entirely due to the relationship of delay time to beam width. (Unless otherwise stated, the numerical values of the antenna and other parameters used in this and later illustrations are those given in the list of symbols.)

Having obtained the impulse response, we turn to obtaining the power and echo cross product through the convolution (17). In pulse-limited altimetry, an asymptotic evaluation [20] of this convolution integral is widely used in practice, based essentially on the assumption that the pulse duration is very much less than the echo duration. This assumption is of limited use in the present case, because, as Fig. 5 shows, the behavior of the impulse response is very much more complex than that of the pulse-limited case. It may be used as $\tau \rightarrow \infty$, and in this case

$$\begin{aligned} \left. \begin{aligned} p_r^{(1)}\left(\tau + \frac{2r_m}{c}\right) \\ \Psi^{(1,2)}\left(\tau + \frac{2r_m}{c}\right) \end{aligned} \right\} &\sim p_0 \tau_p \frac{1}{4\pi} (\sigma^0 + \sigma_v^0) \\ &\cdot \left\{ \begin{aligned} \chi\left(\tau + \frac{2r_m}{c}, 0\right) \\ \chi\left(\tau + \frac{2r_m}{c}, B\right) \end{aligned} \right\} + \left\{ \begin{aligned} p_n \\ 0 \end{aligned} \right. \tau \rightarrow \infty \end{aligned} \quad (28)$$

showing that the trailing edges of power and cross product follow that of the impulse response. Beyond this, it seems one

has to perform a double numerical integral to determine the echo in the general case.

There is one other approximation that is of some use. If one returns to (17) and (18), one may perform the convolution of (17) prior to the surface integration of (18). If one works that way, limits oneself to the power, from a spherical surface, ignores the antenna gain, and supposes that the beam determines the effective illuminated area in the along-track direction, and the transmitted pulse in the across-track direction, consider only zero look angle, and makes the final assumption that the beam is very narrow [the “line” beam discussed following (25)] one may obtain

$$p_r^{(1)}(0) \sim \frac{\lambda^2 G^2 p_0 \sigma^0 \Gamma\left(\frac{5}{4}\right) D_0 \zeta_b}{32\pi^3 h^2} \sqrt{\frac{c\tau_p}{\kappa h}} \quad (29)$$

for the power at zero delay. Here Γ denotes the Gamma function.

An important system parameter in connection with the echo power is the SNR. In fact, for the system considered in this paper, there are three such ratios of interest. The SNR of the pulse-limited echo prior to the beam formation r_{pl} is of importance if the beam formation is done on ground, because it is the SNR that is relevant to onboard control of the echo gating and gain. For the pulse-limited system, the noise power is independent of τ , and we define r_{pl} as the ratio of the signal power that would result were the antenna gain isotropic to the pulse-limited noise power. Combining (26) and (28), one may write for the noisy, mean, pulse-limited echo

$$p_r^{(1)}(\tau) \sim \frac{\lambda^2 G^2 p_0 c \tau_p \sigma^0}{64\pi^2 h^3 \kappa} \left(e^{-2c\tau/\gamma_a^2 h} + r_{pl}^{-1} \right), \quad \tau \gg \tau_p. \quad (30)$$

(This equation defines the pulse-limited noise power as a linear function of the signal power. This is perhaps unconventional but is the most useful representation if one is concerned with the application, rather than the design of the system. With r_{pl} known for a given σ^0 , it is then easy to appreciate the SNR over other surfaces whose backscattering coefficient is known from historical data.)

The second SNR of interest is that of an echo following the beam formation. As (30) illustrates, in an actual measurement the pulse-limited SNR is in detail a function of τ , and the next section shows the SNR following the beam formation is also a strong function of delay and look angle. It is nonetheless useful to characterize it by a single number. One may define a SNR r_{sl} (“sl” is “single look”) as the ratio $p_r^{(1)}(0)/p_n$ for a beam directed normally to a spherical surface. p_n may be written in terms of the pulse-limited noise power using (30) and the fact that it differs from that of the pulse-limited system by the noise power gain D_e of the coherent processing. Together with the approximation of (29), one then has

$$r_{sl} \sim \left[\frac{2\Gamma\left(\frac{5}{4}\right) \zeta_b}{\pi} \sqrt{\frac{h\kappa}{c\tau_p}} \right] \frac{D_0}{D_e} r_{pl} \quad (31)$$

which expresses r_{sl} in terms of r_{pl} . Finally, there is the SNR following the multilooking r_{ml} , which is the SNR that will affect most uses of the measurements. We have not found a simple expression for this; it will be discussed further in Section IV.

In the next sections, the behavior of the echo power and cross product is pursued numerically. We close this section with a brief summary of what has been achieved thus far. Section II-A laid out a number of geometric approximations that, essentially, restricted all angles of interest to lie within a narrow region of the nadir direction [(5)], and restricted the actual scattering surface to have a limited fluctuation about the spherical reference surface [(7)], within that range of angles. These approximations allow the separation of the problem into one that contains the “horizontal” aspects of the problem (the impulse response), and a second, the “vertical” aspects, that all enter the final result through the convolutions of (17). The horizontal problem is reduced to that on a plane, and the geometrical complexity reduced to that of the circles and lines illustrated in Fig. 4. In general the approximations reduce the problem of determining the echo and its cross product to a double integral.

While the geometrical approximations of Section II-A were identified, they were not (in this paper) justified. Some *a posteriori* remarks may be useful. This is simplest done by considering the case $R \rightarrow \infty$. In this case, (9) describes, within the limited range of illumination angles γ_a , a plane surface. The geometric approximations we made are illustrated by considering the exact expressions for the minimum range and its projection onto the equatorial plane, namely, $h \cos \theta_p$ and $h \sin \theta_p \cos \theta_p$ respectively. These may be compared with (11) and (20). One finds that our approximations are good to $O(\theta_p^4)$ in the range, but only $O(\theta_p^2)$ in the horizontal, and the choice of approximations we have made reflect that normal-incidence altimeters are considerably more sensitive to changes in the vertical than the horizontal. See [17] for a closer discussion. Finally, one may also note that, while Brown [20] did not use the Fresnel approximation of (7) directly, (26) is his result. Thus, the approximations made here are consistent with those used historically in pulse-limited radar altimetry.

III. SLANT-RANGE-CORRECTED ECHOES

In practice, a radar does not measure an ensemble mean but must form an estimate of the ensemble mean by averaging a number of individual outcomes, the so-called “looks.” In the present concept, each look is supposed to originate from the surface effectively illuminated by the combination of the gains of the antenna and the along-track beam. As the altimeter moves around the orbit, the look angle may be selected so as to select, from the illuminated strips, the echo from a particular strip. This concept is illustrated in Fig. 1. However, Section II shows that the mean echo is a function of ξ_b , and this variation must be accounted for in describing the ensemble mean of the average of the looks. A part of this variation with ξ_b is the pure delay that is evident in Fig. 5, and this variation in delay may be removed by a “slant-range correction.” To describe the correction more precisely, it is necessary to distinguish between the earth-fixed and satellite-fixed parts of the problem, which is done in Section III-A. The correction itself is described in Section III-B. Even with the correction, there is still a variation in the shape and phase of the mean echoes as a function of the look angle, and this variation is illustrated in Section III-C.

A. Satellite- and Earth-Fixed Reference Frames

To describe the behavior of the echoes from a fixed location on earth, the results of Section II cannot be used without modification. In that section, the reference frame is attached to the satellite (in detail, the center of the interferometer baseline), and so too is the description of the surface. It is necessary now to distinguish between an earth-fixed frame in which the surface is fixed, and a satellite-fixed frame in which the surface is variable. For this purpose we introduce an earth-fixed spherical frame of radius R , and designate any point on the sphere by the polar and azimuthal angles θ_E and λ_E . We now suppose that the scattering surface is described by the normal elevation above the sphere

$$z_E(\theta_E, \lambda_E) = R \sin \theta_E \tan \theta_p \cos(\lambda_E - \lambda_p). \quad (32)$$

This surface passes through the sphere at the point $\theta_E = 0$.

We suppose that the satellite orbit is circular, planar and centered on the earth-fixed sphere. It maintains a constant altitude h above the sphere, and its location is then specified by the earth-fixed coordinates θ_s and λ_s of the nadir point N in Fig. 2. Since the orbit is planar we may assume without loss that $\lambda_s = \pi$ or $\lambda_s = 0$ according to whether the satellite is approaching or has overflown the point $\theta_E = 0$. In what follows, however, this will remain implicit.

To use the results of the previous section, the scattering surface must be described in the satellite fixed coordinates. This is complicated in general, but to the same order of approximation as the previous section, one has

$$\begin{aligned} z_S(\theta, \lambda) &= z_E(\theta_E(\theta, \lambda), \lambda_E(\theta, \lambda)) \\ &\sim R \tan \theta_p (\sin \theta_s \cos(\lambda_s - \lambda_p) \\ &\quad + \sin \theta \cos(\lambda - \lambda_p)). \end{aligned} \quad (33)$$

On comparing this expression for z_S with that of (9) for z , one sees that the two surfaces are the same, save that z_S is offset in the vertical from z by the amount $R \sin \theta_s \tan \theta_p \cos(\lambda_s - \lambda_p)$. Thus, all of the results of the previous section may be applied to the present case, provided one introduces this offset. In fact the effect is simply to replace the minimum range r_m with the function

$$r_{mS}(\theta_s, \lambda_s) = h - R \sin \theta_s \tan \theta_p \cos(\lambda_s - \lambda_p) - \frac{h}{2\kappa} \tan^2 \theta_p. \quad (34)$$

To the same order of approximation, the parameter u_m is unchanged. With reference to Fig. 4, and now considering the line of maximum beam gain as fixed, the effect of the satellite motion is to move the remainder of the figure to the right. What is then apparent is that, whatever the position of the satellite, the earliest appreciable part of the echo as defined by (27) coincides with the same location on the surface. In forming the average of the looks, the aim is to alter the echo delay as a function of position so as to bring the earliest part of the echo into coincidence.

B. Slant Range Correction

One part of the variation in echo delay with look angle is known *a priori* from the geometry of the satellite and the reference figure. This known part is illustrated in Fig. 6. With reference to this figure, an echo from the point S lying at (θ_E, λ_E) on the satellite track (i.e., $\lambda_E = \pi$ or $\lambda_E = 0$) received at the

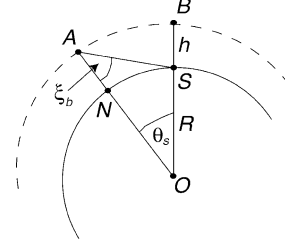


Fig. 6. Geometry of the “slant-range correction.” As the altimeter moves along its orbit, an along-track beam pointed at S may be selected by the processor by its choice of look angle ξ_b . In doing so, the delay time of an echo in traveling from A to S and back also varies. The slant range correction advances the delay of the echo received at A so as to make it equal to the delay resulting from an echo traveling from the point B to S and back.

satellite location A lying at θ_s will be delayed relative to that received at B . To the same order of approximation as previously, this additional delay is

$$\tau_{sl}(\theta_s, \lambda_s, \theta_E, \lambda_E) = \frac{\kappa h}{c} \sin^2 \xi_b. \quad (35)$$

If, in forming the average of the looks at the “strip” passing through the point S , the echoes are advanced by τ_{sl} , the earliest appreciable part of the echo will occur at a time

$$\begin{aligned} t_p &= \frac{2r_{mS}(\theta_s, \lambda_s)}{c} + \tau_{sl}(\theta_s, \lambda_s) + \frac{h\kappa\xi_{mb}^2}{c} \\ &\sim \frac{2h}{c} - \frac{2R}{c} \tan \theta_p \sin \theta_E \cos(\lambda_E - \lambda_p) \\ &\quad - \frac{h}{c\kappa} \tan^2 \theta_p \sin^2 \lambda_p \end{aligned} \quad (36)$$

using (20), (23), (34), and (35) and to the same order of approximation as previously. This time is independent of the position of the satellite. It is equal to the arrival time of the earliest part of the echo that arises when the altimeter is located at the point B in Fig. 6 and the beam is directed at S . The slant range “correction” (i.e., the advance by τ_{sl}) thus achieves the aim of bringing into temporal coincidence the component of each echo corresponding to that part of the surface.

The slant range correction contains no terms that depend on the particular form of the surface z_E . In fact, the key assumption that permits its successful application is the Fresnel approximation of (7). One may show that for any surface for which this approximation holds good the correction of (35) brings into temporal coincidence the echo from any scattering element lying normally above the meridian passing through the point S in Fig. 6 and orthogonal to the orbit. (This is most easily shown by considering a point scatterer, rather than, as here, a surface.) What makes the earliest appreciable arrival of particular importance is that it is unique; more generally more than one element of the surface above the meridian will map to same echo delay. What is special to the particular surface used here is the delay time [(36)] at which this earliest appreciable arrival occurs.

The dependence on θ_E of the delay of earliest appreciable arrival is simply that associated with the elevation of the surface above the sphere at the point B in Fig. 6. In what follows, we shall restrict interest to the point on the surface lying at $\theta_E = 0$; the result for any other point on the ground track is related to that for $\theta_E = 0$ by a simple delay.

We make use of the normalized advanced functions

$$\left. \begin{aligned} &slp_r^{(1)}(\tau, \theta_s, \lambda_s) \\ &sl\Psi^{(1,2)}(\tau, \theta_s, \lambda_s) \end{aligned} \right\} = \frac{128\pi^3 h^3 \kappa}{\lambda^2 G^2 D_0 p_0 c \tau_p \sigma^0} \cdot \left\{ \begin{aligned} &p_r^{(1)}\left(\tau + \frac{2r_{mS}(\theta_s, \lambda_s)}{c} + \tau_{sl}(\theta_s, \lambda_s) - \left(\frac{h}{c\kappa}\right) \tan^2 \theta_p \sin^2 \lambda_p\right) \\ &\Psi^{(1,2)}\left(\tau + \frac{2r_{mS}(\theta_s, \lambda_s)}{c} + \tau_{sl}(\theta_s, \lambda_s) - \left(\frac{h}{c\kappa}\right) \tan^2 \theta_p \sin^2 \lambda_p\right) \end{aligned} \right\}. \quad (37)$$

The new notation is simply for brevity, and the leading factor simply arranges for the new functions to be $O(1)$. With these definitions, $\tau = 0$ identifies the earliest appreciable parts of $slp_r^{(1)}$ and $sl\Psi^{(1,2)}$. (In a measurement, the final term in the argument on the right is not known *a priori*, because the surface is not known, and the advance required to cause the earliest appreciable part to occur at $\tau = 0$ will have to be determined from the measurement.)

To describe the mean phase behavior, we also introduce the new function

$$sl\Delta^{(1,2)}(\tau, \theta_s, \lambda_s) = \text{Arg} \left[\exp \left[ikB \left(\frac{u_m}{h} \cos(\lambda_p - \beta_i) - \sin \delta_i \right) \right] sl\Psi^{(1,2)}(\tau, \theta_s, \lambda_s) \right] \quad (38)$$

that describes the departure of the mean phase from that associated with the earliest appreciable part of the echo arrival when the altimeter is at the point *B* in Fig. 6. As the discussion of the slant range correction implies, this part of the echo comes from the surface element lying a distance $u_m \sin(\lambda_p)$ from the nadir point. With $\beta_i = \pi/2$ and $\delta_i = 0$, and the simplifications of Section II, the exponential function on the right-hand side of (38) removes from the phase of $sl\Psi^{(1,2)}$ that associated with this element of the surface. In short, the phase departure describes the departure of the phase from that deduced by geometric optics.

C. Single-Look Echoes

The normalized, slant range corrected, echo power from a spherical surface is shown in Fig. 7. In contrast to the echo received by a conventional, pulse-limited altimeter, the echoes have a distinct maximum that occurs very shortly after $\tau = 0$, the time we have designated the “earliest appreciable part.” The figure illustrates seven look angles. The first of these, $\xi_b = 0$, designates the case in which the beam is directed at the nadir point (i.e., the altimeter is at location *B* in Fig. 6). This echo corresponds to the most leftward of the impulse responses in Fig. 5. In this case, the impulse response is strictly zero for $\tau < 0$, and the energy that appears in the echo for $\tau < 0$ is due to the finite duration τ_p of the transmitted pulse.

In this example, (29), with (37), provides an estimate for $slp_r^{(1)}(0)$ of 0.949. The numerical integration in Fig. 7 provides a value at $\tau = 0$ of 0.951, showing that (29) is a good approximation, and therefore that (31) a good estimate of the single-look SNR.

As the look angle increases, the maximum power is reduced, and the energy that appears for $\tau < 0$ is increased. This is in part due to the spread in delay time across the beam that is apparent in the impulse responses of Fig. 5; energy that occurred in those prior to the delay $\tau = h\kappa\xi_{mb}^2/c$ is mapped by the slant

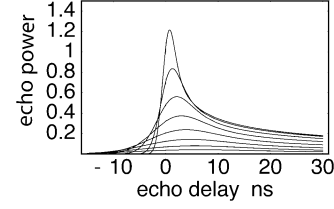


Fig. 7. Mean slant-range-corrected echo power $slp_r^{(1)}$ from a spherical surface for the sequence of look angles $\xi_b = (0, 2, 4, 6, 8, 10, 12) \times 10^{-3}$ rad. Increasing look angle corresponds to a smaller maximum. The transmitted pulse duration is 1.5×10^{-9} s.

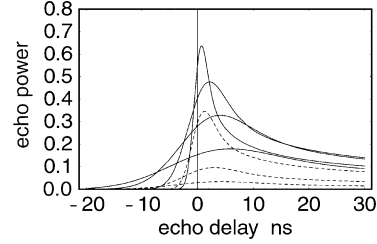


Fig. 8. Mean slant-range-corrected echo power $slp_r^{(1)}$ from a surface inclined to the sphere as described in the text for the sequence of look angles $\xi_{mb} = (0, 2, -4, 6, -8, 10, -12) \times 10^{-3}$ rad. Positive values of ξ_{mb} are shown dashed, zero and negative values as a solid line. Increasing magnitude of ξ_{mb} corresponds to a decreasing maximum.

range correction to energy at $\tau < 0$. The effect in the echoes is more subdued than is the case with the impulse responses due to the smoothing effect of the finite pulse duration. However, this accounts for only some of the reduction in maximum value seen in Fig. 7. This figure shows a considerably wider range of values of ξ_b than was the case for Fig. 5, and some of the reduction in magnitude, particularly at larger values of ξ_b , is due to the axis of the beam falling increasingly far from the antennas’ boresight direction.

The normalized, slant range corrected power from a surface inclined with respect to the sphere in the along- and across-track directions is shown in Fig. 8. For this case, the surface’s departure from a sphere [see (9)] is described by $\theta_p = 7.07 \times 10^{-3}$ rad and $\lambda_p = \pi/4$. The point of closest approach of the surface to the satellite lies forward and to the left of the satellite track (much as is drawn in Fig. 4), and the projected displacement u_m of this point from the nadir point has a value of 4.28×10^3 m. For this example $\xi_{mb} = \xi_b - 5 \times 10^{-3}$ rad, so $\xi_{mb} = 0$, which describes the beam passing through the point of minimum range, corresponds to a look angle of 5×10^{-3} rad.

Fig. 8 shows the mean powers for the sequence of look angles described by $\xi_{mb} = (0, 2, -4, 6, -8, 10, -12) \times 10^{-3}$ rad. Overall, the magnitude of the echoes is reduced with respect to the spherical case illustrated in Fig. 7, and, unlike the case of the spherical surface, the echo is not symmetric with respect to the sign of ξ_{mb} . These are a consequence of the antenna pattern: $\xi_{mb} = 0$ describes a beam at an angle of 5×10^{-3} rad to the antenna boresight direction, and negative values of ξ_{mb} describe beams whose direction is closer to the antenna boresight direction than the corresponding positive value of ξ_{mb} . Nonetheless, in comparing Figs. 7 and 8, one sees that, amplitudes apart, the echoes shapes are very similar. This illustrates that the contribution of the antenna gain to the echo shape is slowly varying

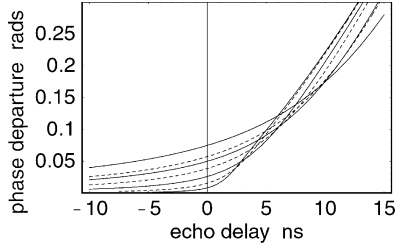


Fig. 9. Phase departure $_{sl}\Delta^{(1,2)}$ of the echo cross product $_{sl}\Psi^{(1,2)}$ from a surface inclined to the sphere as described in the text for the sequence of look angles $\xi_{mb} = (0, 2, -4, 6, -8, 10, -12) \times 10^{-3}$ rad. Positive values of ξ_{mb} are shown dashed, negative values as a solid line. Increasing magnitude of ξ_{mb} corresponds to an increasing value at $\tau \rightarrow 0$.

in comparison with that of the beam gain; the antenna gain determines the overall magnitude of the echo but has little effect on its rapid variation with delay time.

In contrast to the spherical surface, Fig. 8 shows the echoes from a surface whose gradient has an across-track component. Fig. 9 shows the corresponding sequence of the phase departure function $_{sl}\Delta^{(1,2)}$. If one considers only the case of $\xi_{mb} = 0$, the phase response is essentially similar to that described in [14] notwithstanding that in this case the surface gradient has an along-track component. The phase departure is, essentially, zero for $\tau < 0$, and has, again essentially, a linear dependence on for $\tau > 0$. For $\tau < 0$, the phase behavior reflects that the power in this region of the echo is arriving from the earliest detectable part of the surface. For $\tau > 0$, the behavior may be understood with reference to Fig. 4. As τ increases, the echo power is increasingly the sum of contributions from two distinct regions, lying around the two intersections of an isorange circle with the line of maximum beam sensitivity, and these regions are increasingly asymmetrically weighted by the antenna pattern as τ increases. The consequence is that the phase is increasingly weighted in the direction of the region closer to the antenna boresight.

As $|\xi_{mb}|$ increases, however, the distinction between $\tau > 0$ and $\tau < 0$ becomes blurred. The cause of this behavior is the broadening of the impulse response with ξ_{mb} that is apparent in Fig. 5. The slant range correction can only exactly superimpose contributions to the echo from points lying on the line of maximum beam gain. Points lying within the beam, but side-to-side of the maximum, are not mapped to exactly the same arrival time, and the sharp distinction of the $\xi_{mb} = 0$ case is lost. Beams falling some way from the point of minimum range have a phase behavior that is distinctly curved.

IV. MULTILOOKED ECHOES

An individual echo from single look suffers a fluctuation that causes it to depart considerably from the mean shape described in Section III. The purpose of multilooking is to reduce this fluctuation by summing over the look angle the echoes arising from any particular “strip” on the surface. In the present case, in which the mean echo varies with the look angle, the multilooked echo, and its residual fluctuations, are somewhat different from that associated with multilooking an echo with a fixed mean. Therefore, in this section, we describe the mean and statistics

of the multilooked echo. Section IV-A defines the multilooked echo and introduces the “effective” number of looks and phase coherence that arises in this case. Section IV-B provides some illustrations of the multilooked echo and its behavior.

A. Effective Number of Looks and Coherence

For any given point on the satellite ground track ($\theta_E, \lambda_E = \pi$ or $\lambda_E = 0$) and at any single-look angle, the altimeter will obtain the two, complex echoes $\Phi^{(1)}$ and $\Phi^{(2)}$. For brevity, we denote the slant range corrected form of these echoes [i.e., the form obtained by advancing the echoes in the manner of (37)] by $_{sl}\Phi$. From these two echoes a single-look power and cross product are determined

$$\left\{ \begin{matrix} m_l \Omega^{(1)} \\ m_l \Sigma^{(2)} \end{matrix} \right\} (\tau, \theta_{sk}, \lambda_{sk}, \theta_E, \lambda_E) = \sqrt{\frac{128\pi^3 h^3 \kappa}{\lambda^2 G^2 D_0 p_0 c \tau_p \sigma^0}} \cdot \left\{ \begin{matrix} _{sl}\Phi^{(1)}_{sl}\Phi^{(1)} \\ _{sl}\Phi^{(1)}_{sl}\Phi^{(2)} \end{matrix} \right\} (\tau, \theta_{sk}, \lambda_{sk}, \theta_E, \lambda_E). \quad (39)$$

Multilooking describes the averaging of these powers and cross products over the look angle to form a single echo power $_{ml}\Pi^{(1)}$ and cross product $_{ml}\Xi^{(1,2)}$ for each location on the ground track

$$\left\{ \begin{matrix} m_l \Pi^{(1)} \\ m_l \Xi^{(1,2)} \end{matrix} \right\} (\tau, \theta_E, \lambda_E) = \frac{1}{N} \sum_k \left\{ \begin{matrix} _{sl}\Omega^{(1)} \\ _{sl}\Sigma^{(2)} \end{matrix} \right\} (\tau, \theta_{sk}, \lambda_{sk}, \theta_E, \lambda_E). \quad (40)$$

Here N is the total number of looks. The means of these quantities are then

$$\begin{aligned} m_l P_r^{(1)}(\tau, \theta_E, \lambda_E) &\equiv E \left\{ m_l \Pi^{(1)} \right\} \\ &= \frac{1}{N} \sum_k _{sl} P_r^{(1)}(\tau, \theta_{sk}, \lambda_{sk}, \theta_E, \lambda_E) \\ m_l \Gamma^{(1,2)}(\tau, \theta_E, \lambda_E) &\equiv E \left\{ m_l \Xi^{(1,2)} \right\} \\ &= \frac{1}{N} \sum_k _{sl} \Psi^{(1,2)}(\tau, \theta_{sk}, \lambda_{sk}, \theta_E, \lambda_E). \end{aligned} \quad (41)$$

The quantity

$$_{ml}\Lambda^{(1,2)} = \text{Arg} \left[\exp \left[ikB \left(\frac{u_m}{h} \cos(\lambda_p - \zeta_i) - \sin \delta_i \right) \right] m_l \Gamma^{(1,2)} \right] \quad (42)$$

is the mean phase departure [cf. (38)] of the multilooked echo cross product $_{ml}\Xi^{(1,2)}$.

Each echo and echo cross product in the sums of (40) have a different mean, and the reduction in the fluctuations that result are not those normally associated with a number of looks N . With the coefficient μ as defined in (B1), the normalized variance of the multilooked power is

$$\frac{E \left\{ \left(m_l \Pi^{(1)} - E \{ m_l \Pi^{(1)} \} \right)^2 \right\}}{\left(E \{ m_l \Pi^{(1)} \} \right)^2} = \frac{1}{\mu N}. \quad (43)$$

μ is a factor that accounts for the fact that the “effective number of looks” μN is smaller than the actual number of looks N , due to the variation in power as a function of look angle. Generally, $\mu(\tau)$ is a function of delay time, and, also generally, both of N and the look angles themselves. However, if the sampling of the

look angle is dense, the dependence of μ on N and the look angles may be ignored. Provided μN is large, which will be the case in practice, the statistics of the multilooked power may be taken to be Gaussian for practical purposes, in which case (43) defines its statistics completely.

The statistics of the multilooked cross product $_{ml}\Xi^{(1,2)}$, and the phase derived from it, are generally complicated. However, if the number of looks is large, and the coherence fairly high, the situation is greatly simplified, and that is the case we treat here. With a multilooked “coherence” $_{ml}K^{(1,2)}$ defined as in (B4), the variance of the phase measurement is then

$$E \left\{ \left(\text{Arg} \left[_{ml}\Xi^{(1,2)} \right] - E \left\{ \text{Arg} \left[_{ml}\Xi^{(1,2)} \right] \right\} \right)^2 \right\} \sim \frac{(1 - (_{ml}K^{(1,2)})^2)}{2\mu N (_{ml}K^{(1,2)})^2}. \quad (44)$$

Again, if the sampling of the look angle is dense, the dependence of $_{ml}K^{(1,2)}$ on N and the look angles may be ignored, and provided μN is large, the statistics of the multilooked phase may be taken to be Gaussian for practical purposes, in which case (44) defines these statistics completely.

If, as is not the case considered here, the means of the individual looks were equal, then the formula (B1) for μ collapses to $\mu \equiv 1$ and that of (B4) for $_{ml}K^{(1,2)}$ to the conventional expression for the coherence, that is, $_{ml}K^{(1,2)} = |_{sl}\Psi^{(1,2)}| / |_{sl}P_r^{(1)}$ in our notation. In that case, (43) gives the usual, exact formula for the variance of an average of an exponentially distributed fluctuation, while (44) gives the conventional, large N approximation for the phase variance. The large N limit of the approximate formula given by Jensen [14] for the fourth moment of the phase may then be obtained from (44) under the assumption of Gaussian statistics.

In the practical situation, N is made as large as possible, and the sampling density of the look angle very fine indeed. In the examples below we take $N = 30$ with the look angles uniformly distributed across the angular extent of the antenna gain (out to -17 dB); we established (by trial and error) that the effect of further increasing N on the multilooked power and cross product, and thus on μ and $_{ml}K^{(1,2)}$, is negligible.

B. Multilooked Echo Power, Phase, and Coherence

The behaviors of $_{ml}P_r^{(1)}$ for the geometries of Section III-C, that is, of a spherical surface and a surface inclined to the sphere along and across track, are shown in Fig. 10, using the parameter values given in Appendix A. Of these, the most important are an altitude of 0.72×10^6 m, a wavelength of 2.0 cm, a compressed pulse duration of 3 ns ($2\tau_p$), an antenna beam width of 1.25×10^{-2} rad, a beam gain width of 2×10^{-4} rad, and an interferometric baseline of 1.2 m.

The main effect of the multilooking is twofold: the sharpness of the central peak is reduced, and the net effect spreading in delay time for $\tau < 0$ of the beams is to generate a precursor to the rapidly rising part of the leading edge of the echo. The shape of the trailing edge is little affected by the multilooking.

In comparison with the nadir beam of the single-looks (shown in Fig. 7), the magnitude of the multilooked echo is reduced by 5.8 dB, a reduction that reflects in part the reduction across the single-looks due to the broadening of the impulse response seen

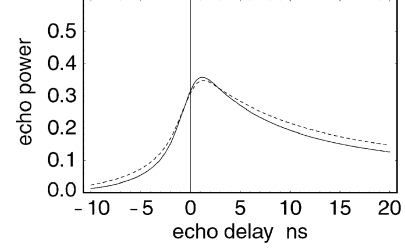


Fig. 10. Multilooked echo power $_{ml}P_r^{(1)}$ from (solid line) a spherical surface and (dashed line) a surface “inclined” to a sphere as described in the text. The power from the inclined surface has been scaled (by a factor 1.5) to bring it into approximate coincidence with that of a spherical surface.

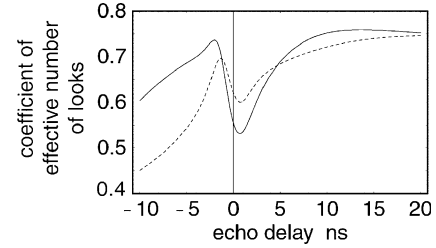


Fig. 11. Coefficient of the effective number of looks $\mu(\tau)$ as a function of echo delay time for (solid line) a spherical surface and (dashed line) a surface “inclined” to a sphere as described in the text.

in Fig. 5, and in part the weighting of the beams by the antenna gain. In Fig. 10 the amplitude of the power from the inclined surface has been adjusted by a factor of 1.7 dB to bring it into coincidence with that of the spherical surface. This is rather less than one would suppose were the difference in the two cases simply due to the antenna gain: for this example, the reduction in power due to the antenna gain in the direction of the point of minimum range is -3.1 dB.

In general, the detailed variation in maximum power of the multilooked echo depends on the surface geometry in a rather complex manner that only seems amenable to a numerical investigation; a direct reflection of our inability to find a useful analytic approximation to (22). This has the consequence that we have not been able to find a usefully general, simple expression for the multilooked SNR r_{ml} . What is clear is that one must be careful of applying to a multilooked echo the single-look SNR estimated by (31). For this example, the single-look SNR is, from (31), $0.15(D_0/D_e)r_{pl}$. On the other hand, with the weightings of (41), $r_{ml} \sim 0.03(D_0/D_e)r_{pl}$. The multilooked SNR r_{ml} is substantially lower than the single-look SNR r_{sl} .

On the other hand, it may be seen that, magnitude apart, the two multilooked echoes are extremely similar; the average echo power is very insensitive to the along or across-track gradients of the surface. This is quite remarkable, given the very marked difference between the along and across-track illuminations.

Somewhat more dissimilar in the two cases is the behavior of the coefficient of the effective number of looks $\mu(\tau)$, illustrated in Fig. 11. If, say, two of the looks had a considerably larger power than any of the other $N - 2$ looks, they would dominate the average of (40) and the resulting fluctuations would very largely be those of two, rather than N looks. μ is a numerical measure of the fractional reduction in the number of looks due to the dissimilarity of the powers. Since the dissimilarity

of powers is a function to delay time, so too is $\mu(\tau)$. Considering the spherical case first, whose individual looks are shown in Fig. 7, the largest values of $\mu(\tau)$ occur for large τ , where the difference from look to look arises solely due to the antenna pattern, and are rather small. The pronounced dip in the vicinity of $\tau = 0$ reflects the increased variation due to the closeness of some beams to the point of minimum range (i.e., beams having a value of ξ_{mb} close to 0). At $\tau = 0$, $\mu(0) = 0.527$, so that, approximately speaking, the effective number of looks is half the actual number. As τ becomes increasingly negative, the effective number of looks falls away, due to the loss in signal power associated with the beams falling close to the point of minimum range. The same overall behavior occurs in the case of the inclined surface, whose individual looks are shown in Fig. 8, but the detailed variation is distinct. At large positive and negative values of τ the variation is rather greater, and $\sqrt{\mu(\tau)}$ is lower, while in the vicinity of $\tau = 0$ the variation is more subdued. At $\tau = 0$, $\mu(0) = 0.585$ the inclined surface has a slightly higher effective number of looks than in the spherical case.

The multilooked phase departure $_{ml}\Lambda^{(1,2)}$ from the inclined surface is shown in Fig. 12. The phases of the corresponding individual looks is shown in Fig. 9. However, $_{ml}\Lambda^{(1,2)}$ is the argument of the average of the single-look echo cross products whose magnitude (not shown) is similar (although not identical) to that of the corresponding powers shown in Fig. 8. and this weighting is apparent in the curve. As τ becomes increasingly negative, weight is given to echoes whose phase is blurred in the fashion described in Section III-C. In the vicinity of $\tau = 0$, echoes from close to the point of minimum range have increased weight, and the curve has a distinct minima. At $\tau = 0$, $_{ml}\Lambda^{(1,2)}(0) = 0.03$ rad. As τ increases, the phase departure is increasingly weighted toward the antenna boresight direction as described in Section III-C.

The behavior of the multilooked coherence $_{ml}K^{(1,2)}$ is illustrated in Fig. 13 for the spherical and inclined surface. The overall behaviors in the two cases are very similar, and arise as follows. The coherence is principally determined by the extent of the across-track distribution of illuminated area. For $\tau < 0$, this is largely restricted to the area in the vicinity of that contributing to the earliest appreciable part of the echo, and the coherence remains high. As τ increases, the echo is increasingly formed from the two distinct regions described in Section III-C, and these are increasingly separated as τ increases and the coherence drops accordingly.

We noted above that the single-look SNR is a poor estimate of the multilooked SNR; the same is true of the coherence. Making the same approximations that led to (29), one may obtain for a narrow beam directed normally to the sphere

$$C(0) \sim 1 - \frac{\Gamma(\frac{3}{4})}{8\Gamma(\frac{5}{4})} \frac{c\tau_p(kB)^2}{h\kappa} \quad (45)$$

as an approximation to the single-look coherence at $\tau = 0$. An essentially similar expression is given in [14]. This expression yields a coherence of 0.985, whereas in fact $_{ml}K^{(1,2)}(0) = 0.974$ in the present example, so that multilooking does degrade the single-look coherence.

Turning now to the distinction between the curves in Fig. 13, the coherence arising from the inclined surface is slightly lower

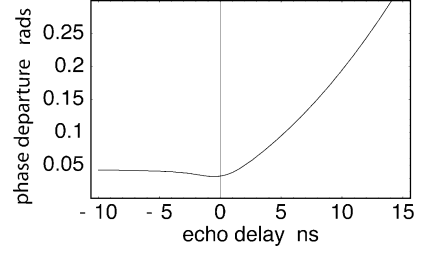


Fig. 12. Multilooked phase departure $_{ml}\Lambda^{(1,2)}$ in radians as a function of echo delay arising from a surface “inclined” to a sphere as described in the text.

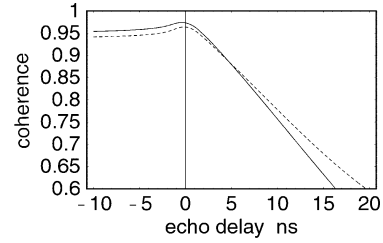


Fig. 13. Coherence $_{ml}K^{(1,2)}$ as a function of echo delay arising from (solid line) a spherical surface and (dashed line) a surface “inclined” to a sphere as described in the text.

in the vicinity of $\tau = 0$ than that arising from a spherical surface, and slightly higher as τ increases. The first of these can be explained geometrically, but only at some length. In short, it arises as a result of the spreading of the impulse response as ξ_{mb} increases, coupled with the increased weighting given to these beams by the asymmetry of the antenna pattern (cf. Fig. 8). The slight increase in coherence as τ increases is more easily explained: the coherence is sensitive to the fact that the distinct contributions to the echo that arise at larger values of τ are differently weighted by the antenna gain, reducing to some extent the “effective” across-track distribution of illuminated area.

V. EFFECTS OF SURFACE ROUGHNESS, VOLUME SCATTERING, AND NOISE

In this section some “perturbations” to the echo power, phase and coherence introduced by the effects of surface roughness, volume scattering and thermal noise are illustrated. Section V-A deals with surface roughness, Section V-B, volume scattering, and Section V-C, thermal noise.

A. Effect of Surface Roughness

The consequence of varying the roughness on the multilooked echo power is illustrated in Fig. 14. This shows the echo power for the sequence of values of the standard deviation of surface roughness $\sigma_s = (0, 0.15, 0.3, 0.45, 0.6, 0.75)$ m. The mean echo is equal to that in the absence of roughness convolved with the roughness distribution, and the effect is to broaden the echo. One feature that is distinct from the corresponding case in pulse-limited altimetry is that the magnitude of the echo in the vicinity of $\tau = 0$ depends on the roughness, a reflection of the more rapid variation with delay time of the impulse response in the present case.

Increasing the surface roughness increases the radius of the pulse-limited footprint, and, as observed in [14], one may anticipate the coherence will fall as a result. [14] describes

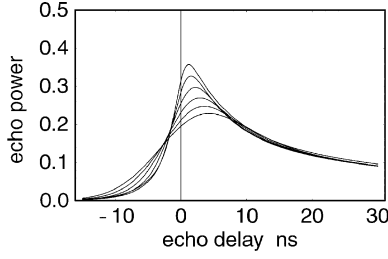


Fig. 14. Multilooked echo power $_{sl}P_r^{(1)}$ from a spherical surface as a function of echo delay for the sequence of delay-equivalent surface roughness standard deviations $\sigma_s = (0, 0.15, 0.3, 0.45, 0.6, 0.75)$ m. Increasing standard deviation corresponds to a smaller maximum.

the roughness dependence of the single-look coherence by the factor $\sqrt{(\tau_p^2 + 2\sigma_s^2/c_2)}$. We have found (not shown) that this dependence also describes reasonably the variation of the multilooked coherence with surface roughness.

Another effect (not shown) of increasing surface roughness is also worth noting. As the pulse-limited footprint becomes large, the antenna weighting makes itself felt on the phase departure even for the beam directed at the point of minimum range (i.e., with $\xi_{mb} = 0$). The “dragging” of the phase departure away from 0 at $\tau = 0$, apparent in Figs. 9 and 12, increases with roughness. (A close look at Fig. 9 shows that the transmitted pulse width is sufficient itself to cause a very small phase offset for $\xi_{mb} = 0$ case at $\tau = 0$, even when the roughness standard deviation is 0.)

B. Effect of Volume Scattering

To consider the effect of volume scattering, we assign to (16) nonzero values of α_v^{-1} and σ_v^0 . Here, we illustrate the case with $\alpha_v^{-1} = 10$ ns (corresponding to a penetration depth of 1.5 m) and $\sigma_v^0 = \sigma^0$, which describes a situation in which the total power scattered from the volume equals that scattered by the surface.

Fig. 15 compares the multilooked power $_{ml}P_r^{(1)}$ from the spherical surface with and without volume scattering. The volume scattering is described by the one sided operator $v(z)$ [in (16)], so the effects of the volume scatter are very largely restricted to positive values of τ . The peak of the echo is somewhat increased, and slightly delayed with respect to the surface-only echo. For values of τ of order of the delay equivalent penetration depth, the trailing edge falls almost linearly with τ . For larger values of τ , the echo shape is similar to that of the surface echo, as required by (28). The difference between the two echoes is then simply that one has twice the power of the other.

We have examined the effect of volume scattering on the echo from the inclined surface and found its effect on the power to be very similar to that shown in Fig. 15. The effect on the multilooked phase (not shown) is to very slightly reduce the phase departure at positive values of τ . The effect is very small, however, and will be negligible in practice.

The effect of the volume scattering on the multilooked coherence is shown in Fig. 16. Comparison of the two curves shows that its effect for $\tau < 0$ and in the vicinity of $\tau = 0$ the volume scattering has very little effect on the coherence—a consequence of the one-sided nature of the volume scattering

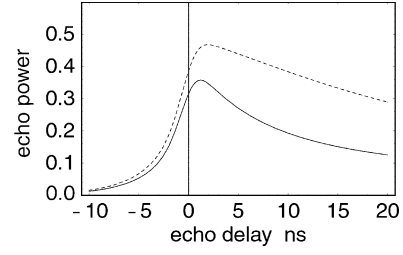


Fig. 15. Multilooked echo power $_{ml}P_r^{(1)}$ as a function of echo delay from (solid line) a spherical surface and (dashed line) a spherical surface underlain by a scattering volume. The total energy of the volume-scattered power equals that of the surface. The delay equivalent penetration depth of the volume is 10 ns.

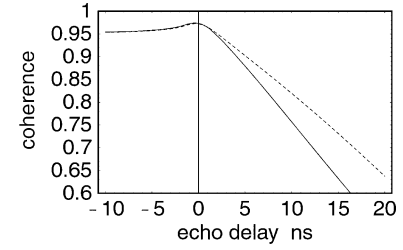


Fig. 16. Multilooked coherence $_{ml}K^{(1,2)}$ as a function of delay time arising from (solid line) a spherical surface and (dashed line) a spherical surface underlain by a scattering volume. The total energy of the volume-scattered power equals that of the surface. The delay equivalent penetration depth of the volume is 10 ns.

operator. For larger values of delay time however, the coherence remains higher than is the case in the absence of volume scattering. As was noted in Section IV-B, as τ becomes large, the contribution of the surface scattering to the echo arises from two distinct regions whose across-track separation increases with τ . Contributions to the echo from the *volume*, however, occur at depth from an across-track distribution everywhere between these two regions. The total effect is to narrow to some degree the “effective” across-track distribution of scatterers, with the result that the coherence is, to a degree, increased.

C. Effect of Thermal Noise

The effect on the mean echo power as a function of delay time of the addition of thermal noise is simply to add to it a constant noise “floor.” This does not need illustration. Thermal noise has no effect in the mean on the phase of the echo cross product. However, thermal noise does strongly affect the echo coherence and the affect is worth illustrating, because this is how the affect appears in a measurement.

Fig. 17 shows the multilooked coherence $_{ml}K^{(1,2)}$ as a function of τ for the sequence of SNRs $r_{ml} = (10, 15, 20, \infty)$ dB. (The case $r_{ml} = \infty$ is repeated from Fig. 13.) Because of the way the parameter is defined, a given value of r_{ml} describes a constant noise floor as a function of τ , as would occur in a measurement. The variation in coherence with SNR seen in Fig. 17 is thus a reflection of the varying signal power as a function of τ . When noise is present, the coherence drops rapidly for increasingly negative τ , corresponding to the rapid drop in multilooked signal power seen in Fig. 10. For positive τ , the multilooked signal power falls less rapidly, and the effect of the noise is more subdued.

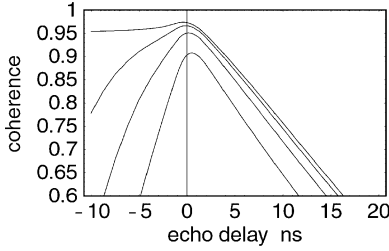


Fig. 17. Multilooked coherence $_{ml}K^{(1,2)}$ as a function of echo delay time, arising from a spherical surface, for the sequence of multilooked SNRs $r_{ml} = (10, 15, 20, \infty)$ dB. Increasing SNR corresponds to increasing coherence.

VI. DISCUSSION

In this section, some implications and limitations of the preceding results for the estimation of elevation of an ice sheet by a practical system are considered. These are illustrated using the parameter values given in Appendix A. Of these, the most important are an altitude of 10^6 m, a wavelength of 2.2 cm, a compressed pulse duration of 3 ns ($2\tau_p$), an antenna beam width of 10^{-2} rad, a beam gain width of 10^{-4} rad, and an interferometric baseline of 1.2 m.

A. Range and Phase Contributions to the Elevation Precision

The essential basis for the measurement of elevation using the interferometric phase has been described in [14] on the basis of the impulse response of a plane surface; the main purpose here is to consider the more realistic situation, and the relative importance of the range and phase errors.

If one constructs a plane orthogonal to the orbit and passing through the nadir point, the intersection of the surface with the plane is a line. If the point on the line closest to the satellite lies at a range r_P from the satellite and subtends at the satellite an angle α_P with the nadir point, the elevation of the point is given by

$$z_P = (r_P^2 + (h + R)^2 - 2r_P(h + R)\cos\alpha_P)^{1/2}. \quad (46)$$

If in making a measurement of r_P and α_P the errors ε_r and ε_α occur in the range and angle, the estimate of elevation z_e that results is

$$z_e \sim h + \frac{h\kappa}{2}\sin^2(\alpha_P + \varepsilon_\alpha) - r_P - \varepsilon_r \quad (47)$$

to the same level of approximation as we have used previously. This estimate is first order in the errors. If, on the other hand, one takes z_e to be an estimate of the elevation of the point on the surface subtending an angle $\alpha_P + \varepsilon_\alpha$ with the nadir point, then, for the particular “plane” surface considered here, one may show that using the results of Sections II and III that

$$z_e - z_E \sim \frac{h\kappa}{2}\varepsilon_\alpha^2 - \varepsilon_r \quad (48)$$

to the level of approximation we are using. In contrast to (47), this error is second order in the angle error. This is because, with the particular surface considered here, the geometry is pulse-limited in the across-track plane, as observed previously [14].

The aim of the measurement system is to use the multilooked echo power to determine the range r_P and the echo phase to estimate the angle α_P . The range r_P is that corresponding to

the delay time t_P of (36); the error ε_r is $c/2$ times the error with which the time $\tau = 0$ is determined from the multilooked echo. If the phase of the multilooked cross product at this delay time is used to estimate α_P , the error that results on average is

$$\varepsilon_\alpha \sim (kB)^{-1} \left(\varepsilon_\Lambda + {}_{sl}\Lambda^{(1,2)}(0) + \frac{2\varepsilon_r}{c} \frac{\partial {}_{sl}\Lambda^{(1,2)}(0)}{\partial \tau} \right) \quad (49)$$

where the interferometer phase error is assumed small enough that the general expression for the angle error may be linearized. In (49), ε_Λ is the random component of the interferometer phase error; the remaining terms are biases.

In detail the range precision ε_r will depend on the method (“retracker”) used to determine the time $\tau = 0$ from the multilooked echo, which is not the subject of this paper. For the purposes of this discussion, we can estimate it by reference to the performance of the present generation of pulse-limited altimeters. These presently achieve a range precision of ~ 2 cm for a ~ 2000 look (1 s) average echo. To apply to the present case we need first to determine the number of looks. This is subject to a number of practical considerations;¹ for the purposes of illustration we take $N = 60$. Second, the form of the impulse response has the result that the echo leading edge gradient is approximately twice that of the pulse limited system. Taking from Section IV-B the value $\mu(0) = 0.527$ to account for the effective reduction in the number of looks, we obtain

$$\sqrt{E\{\varepsilon_r^2\}} \sim \frac{2 \text{ cm} \times \sqrt{\frac{2000}{(60 \times \mu(0))}}}{2} = 7.54 \text{ cm}$$

as an estimate of the standard deviation of the range error of each location on the surface. The corresponding value in delay is 0.5 ns. This number may be compared with the corresponding value for pulse-limited systems over ice sheets. These systems conventionally use 100 looks (20 Hz), and the corresponding range precision is 8.9 cm, i.e., a similar level of precision.

We now consider the bias terms in (49). These arise from the phase departure function, which is illustrated in Fig. 12. With a variation due to the range error of order 0.5 ns, this figure shows that it is the term $_{ml}\Lambda^{(1,2)}(0) = 0.03$ rad that makes the largest contribution. Using (48) and (49), however, we find the resulting elevation error is 4.5 mm. Thus, the fact that the phase departure does not pass exactly through the origin at $\tau = 0$ may be ignored for practical purposes.

Finally, we consider the random phase error. This depends on the coherence, which is a function of the surface roughness and SNR, and, to a much lesser extent, the volume scattering. For illustration, we take the low roughness, high SNR limit, in which case $_{sl}K^{(1,2)}(0) = 0.974$, $N = 60$, and $\mu(0) = 0.527$ in (44). In this case we obtain for the expectation of the first term on the right-hand side of (49) a value of 5 mm. This is negligible in comparison with the magnitude of the second term (7.54 cm).

In short, the elevation precision of the system we are considering is dominated by the range, and not the phase, error. We also anticipate that the elevation precision is similar to that of a conventional, pulse-limited system (the aim of the design being to improve coverage, not precision) over a known surface.

¹For example, CryoSat has two modes. In its SAR mode, $N = 252$. In its SARin mode, for use over the ice sheets, three of every four pulses are used for echo gating control, and $N = 63$.

B. Limitations of the Instrument Description

The instrument system described in this paper is simplified in some ways compared with a practical system, in part because we wished to keep the treatment analytic to the extent we could, and in part to limit the length of the paper. In this section, we comment on the more important of these simplifications. These are: the description of the beam gain, the ignorance of ambiguities the choice of antenna gain, and the choice of compressed pulse shape.

In this paper, the beam gain is restricted first to coherent processing in the along-track direction, and second to unfocussed aperture synthesis. These limit the argument of the beam gain to the form of (12) and are not particularly restrictive. More importantly, the shape of the beam gain is limited to a Gaussian function by (12). This is chosen to allow us to reach (25), (29) and (45). In practice, all of the machinery of beam weighting is available with which to trade off a beam's resolution with its sidelobe level. Generally speaking, the higher the resolution, the less the spreading in delay-time of the "nonnormal" ($\xi_{mb} \neq 0$) beams (i.e., those not orthogonal to the along-track surface gradient), and the smaller the phase departure from the origin in the vicinity of $\tau = 0$ (cf. Fig. 12). On the other hand, when the system operates over the uncertain topography of an ice sheet, there may be advantages in having a low sidelobe level.

A second limitation is the ignorance of ambiguities. The coherent processing will result in a beam gain that is a periodic function of angle. In the practical system, these additional beams, whose maxima are at larger angles to the nadir direction, pass, by design, through the sidelobes of the antenna gain, and are much attenuated. The examples in this paper illustrate surface gradients that are less than the width of the "main lobe" of the antenna gain, and having included them would have had negligible effect. However, it is possible that the echoes from more complex topography may result in significant energy from an additional beam. In a similar fashion, the examples in this paper do not consider what would occur when the across-track surface gradient to exceed the angle at which the interferometer phase difference exceeds $\pm\pi$. Again, energy from these off-nadir directions is strongly attenuated by the antenna gain; nonetheless it may occur in practice. What is true is that the practical echo processing—the "retracker"—will not itself detect whether the echo arises from an ambiguous along-track direction or across-track phase. Some kind of post processing is needed to check the outcome.

The antennas' gain is restricted in this paper to a narrow range of angles about the nadir, which is not particularly restrictive. More importantly, we have assumed for simplicity that the antennas' gain is axisymmetric about their boresight. In a practical system, there is no need to make the antennas axisymmetric; indeed, narrowing the across-track antenna dimension compared with a conventional altimeter will increase the range of angles measured by the interferometer within the range $\pm\pi$. While in detail this will affect the illustrations in this paper, this is less so than might at first appear the case.² The behavior of the multi-

looked echo in the vicinity of $\tau = 0$ is largely determined by the angular width of the beam gain and the transmitted pulse duration; the antenna gain simply determines the SNR. It is this fact that lies behind the remarkable insensitivity of the echo shape to surface gradient that is seen in Fig. 10.

Finally, we have also assumed a Gaussian behavior for the transmitted pulse. This allows us to make some small analytic steps [(29) and (45)]. This will effect to some extent the slope of the rising edge of multilooked echo, and the SNR. However, as Fig. 10 shows, the multilooking over the "nonnormal" beams also significantly affects the leading edge slope, and the behavior at large negative values of τ . We would not expect the inclusion of a more realistic transmitted pulse shape to greatly alter the illustrations of the paper.

C. Limitations of the Scattering Model

The scattering model used in this paper [(15) and (16)] ignores some known features of ice sheet scattering. Ice sheets contain unknown topography that results in a considerably increased variability in the estimated range even for pulse-limited systems (a typical number might be 50 cm) and the same will be true of the system considered here. It is also true that this topography may have an increased effect on the present system, because of the increase of the resolution of the beams and the complexities introduced by the multilooking. Aside from this topography, which is the muted result of variations in basal topography, wind-generated surface features such as sastrugi may be distinctly anisotropic. Because pulse-limited altimeters integrate azimuthally, the affect of any anisotropy is undetectable, but this may no longer be true when the relation of the resolution cell of the instrument to the surface depends on the flight direction. (The same may also be true of the way the echo from the ocean is affected by ocean swell.) This means that the retrieved range may depend on the satellite direction.

Separately from this, the volume scattering from ice sheets, even at near normal incidence, is a function of the flight direction [18], a result, presumably, of the sensitivity of the scattering to the polarization of the transmission and an anisotropy in the grains, or layers, that comprise the firn. In pulse-limited altimetry of ice sheets, this sensitivity to flight direction may add an error of some 50 cm to the estimated range. It is not easy to estimate a corresponding figure for the system described here.

For all these reasons, it is unlikely that over an ice sheet, the precisions of 8 cm (20 Hz) described in Section VI-A above will be achieved. Errors of 50 cm, and spatial or temporal variability of 50 cm are to be expected. This said, the most important geophysical use of ice altimetry is not to estimate the elevation, but the change in elevation, for it is this quantity that bears on the exchange of ice sheet mass with the ocean. Errors that are independent of time are easily removed from the measurements of change, and with pulse-limited systems this includes errors arising from uncertain topography and from azimuthal variation in volume scattering, but errors from variations in the surface geometry remain. It is likely that the same will be true of the system described here.

²The CryoSat antennas are, for reason of accommodation rather than performance, 1.4 m \times 1.15 m. This small asymmetry will not greatly effect the results of this paper.

VII. CONCLUSION

In this paper we have examined the concepts of a beam-forming [13] and interferometric [14] altimeter with a view to determining the performance when a number of complexities of the actual situation, and in particular the multilooking, are considered in detail. For this purpose we have extended the description of the rough surface impulse response and corresponding echo to include geometries with an along and across-track slope, and consider beam directions at an angle ξ_{mb} to the along-track surface gradient. The effect of beams with finite values of ξ_{mb} is the extension in delay time, and reduction in power, of the “nonnormal” ($\xi_{mb} \neq 0$) beams. In addition, the interferometric phase differs from beam to beam, and no longer conforms, in detail, to that deduced from geometric (i.e., ray-optic) considerations.

As a consequence of the variation with ξ_{mb} of the beams, the multilooked echo differs in detail in a number of respects from a single “normal-incidence” beam. The peak of the echo power is less pronounced, and a precursor “toe” is present as a result of the extension to earlier delay times of the nonnormal beams. The interferometric phase also departs from that deduced on a geometric basis as a result of the nonnormal beams. Because the beams that form the multilooked echo are drawn from different statistical ensembles, the usual measures of their power and phase fluctuations need modifying: in particular the “effective” number of looks is less than the actual number of looks, and the definition of coherence needs modifying if the usual formula is to be used to estimate the phase statistics. The suitably modified coherence is lower than would be obtained from calculations based on the “normal” beam, principally due to the reduction in the effective number of looks. Its dependence on the surface roughness and SNR is similar to that obtained from simpler geometric considerations, but differs in detail. We have also examined the effect of volume scattering on the multilooked echo, and found that while it alters the echo power, it has little affect on the rising edge of the echo power, or on the coherence at small delay times.

For the parameters of the practical system examined here, an initial examination shows that the departures of the multilooked echo and echo product from the more ideal cases considered by Raney [13] and Jensen [14] are of the orders of millimeters, and too small to effect the measurement precision in practical applications. This initial examination also shows that in practice it is the range precision, rather than the phase precision that will dominate the measurement error. A more detailed examination is needed, particularly of the range estimation, and some practical problems remain to be solved. These arise in the main because we have not been able to provide a usefully accurate closed form for the multilooked echo. The dependence of the multilooked echoes on the surface parameters is less explicit, and more variable, than is the case with pulse-limited systems. In principle, this may be overcome by pulse-fitting, but there are practical difficulties to this when the dependence of the echo on any one of six parameters is only known through a double numerical integral and a summation. Jensen [21] proposed overcoming the problem of variation by operating on the echo with a linear operator that returns the echo to a pulse-limited form.

This solution has clear merit when the echo shape is known in detail *a priori* (although the detailed form of the operator will be more complex than that described by Jensen once multilooking is accounted for). However, over the ice sheets, where the detailed topography is not known *a priori*, there may well be merit in a more empirical approach, similar to those used in the past with pulse-limited systems.

Past experience with pulse-limited systems also lead us to expect that errors will occur in the elevations arising from the unknown ice sheet topography, and azimuthal dependencies of the surface and volume scattering. Any investigation of these must wait on the “retracker” design. Even with this, however, these issues are difficult to investigate numerically, in part because the coherent nature of the system makes a numerical simulation of the consequences of scattering variability a considerable undertaking, and in part because there is only limited theoretical understanding of the causes of the variation in the firm. It is probably more useful, and certainly easier, to investigate these matters empirically with actual measurements.

APPENDIX A

LIST OF NOTATION, SYMBOLS, AND NUMERICAL VALUES

$E\{x\}$	expectation of x ;
\bar{x}	complex conjugate of x ;
POCAINP	point of closest approach in nadir plane;
B 1.2 m	interferometer baseline length;
C	single-look coherence;
c 3×10^8 ms ⁻¹	speed of light in air;
c_v	speed of light in scattering volume;
d	power sensitivity of along-track beam;
D_e	noise power gain of coherent beam processing;
D_0	peak power sensitivity of along-track beam;
g	one-way antenna gain;
G	peak one-way antenna gain;
h 0.72×10^6 m	satellite altitude;
I_0	modified Bessel function;
$k = \omega_0/c$ 314 m ⁻¹	wavenumber of carrier wave;
k_e	two-way volume extinction coefficient;
k_t	transmission coefficient at surface;
$_{ml}K^{(1,2)}$	multilooked coherence; see (B4);
$\hat{\mathbf{m}}_b$	unit vector in direction of interferometer baseline;
$\hat{\mathbf{n}}$	unit vector in nadir direction;
$\hat{\mathbf{n}}_r$	unit vector in direction of scattering element;
$\hat{\mathbf{n}}_v$	unit vector in direction of satellite velocity viewed from earth;
N	number of looks;
p_0	peak transmitted power;
p_t	transmitted (pulse compressed) power envelope;
p_n	noise power;

$p_r^{(1)}, p_r^{(2)}$	mean echo power at left and right antennas;	σ_v^0	total volume backscattering coefficient per unit surface area; see (16);
$_{st}p_r^{(1)}$	single-look mean echo power at left antenna;	ρ	angle between $\hat{\mathbf{n}}_r$ and $\hat{\mathbf{m}}_b$ (see Fig. 3);
$_{ml}P_r^{(1)}, _{ml}P_r^{(2)}$	multilooked, mean power at left and right antennas;	μ	coefficient of the effective number of looks;
r_m	minimum distance from satellite to surface;	θ, λ	polar and azimuthal coordinates in satellite-fixed frame (see Fig. 2);
r_{mS}	see (34);	θ_E, λ_E	polar and azimuthal coordinates in earth-fixed frame;
r_{pl}	pulse-limited SNR;	θ_s, λ_s	satellite coordinates in earth-fixed frame;
r_{prp}	range to POCAINP;	$\theta_{sk}, \lambda_{sk}$	see (39);
r_{sl}	single-look SNR;	θ_p	angular gradient of the surface;
r_{ml}	multilooked SNR;	ϑ	azimuthal coordinate (see Fig. 4);
\mathbf{r}	vector joining satellite and scattering element;	λ_p	azimuthal direction of surface gradient;
$R 6 \times 10^6$ m	radius of the sphere;	τ	echo delay advanced by $2r_m/c$;
s	surface roughness density function;	$\tau_p 1.5 \times 10^{-9}$ s	transmitted pulse duration;
t	echo delay from instant of transmission;	τ_{sl}	delay associated with the slant range correction;
t_p	time of earliest part of echo;	$\omega_0 9.4 \times 10^{10}$ rad \cdot s ⁻¹	radian frequency of carrier wave;
u_m	see (20) and Fig. 4;	$\Psi^{(1,2)}$	mean cross product of echoes;
v	vertical scattering distribution function (16);	$_{st}\Psi^{(1,2)}$	mean single-look echo cross product;
z	elevation in satellite-fixed frame;	$_{st}\Delta^{(1,2)}$	mean single-look phase departure; see (38);
z_E	surface elevation in earth-fixed frame;	$_{ml}\Lambda^{(1,2)}$	mean multilooked phase departure; see (42);
z_e	estimated surface elevation;	$_{ml}\Pi^{(1)}, _{ml}\Pi^{(2)}$	multilooked coherent echoes at left and right antennas; see (43);
z_S	scattering surface in satellite coordinates;	$_{ml}\Gamma^{(1,2)}$	mean multilooked echo cross product;
α_v	attenuation coefficient; see (16);	$\Phi^{(1)}, \Phi^{(2)}$	coherent echoes at the left and right antennas;
α_p	angle between direction of POCAINP and $\hat{\mathbf{n}}_n$;	$_{st}\Phi^{(1)}, _{st}\Phi^{(2)}$	see (39);
β_i	azimuthal coordinate of the baseline vector;	χ	impulse response; see (18);
β	azimuthal coordinate of the vector $\hat{\mathbf{n}}_r$;	$_{st}\Omega^{(1)}$	single-look power;
δ_i	interferometer roll angle;	$_{st}\Sigma^{(1,2)}$	single-look cross product;
ε_a	measurement error of α_P ;	$_{ml}\Xi^{(1,2)}$	mean multilooked echo cross product.
ε_r	measurement error of r_p ;		
$\varepsilon_r Z_p$	elevation of POCA in nadir plane;		
ε_Λ	random component of measurement error of $\alpha_p Z_p$;		
$\kappa 1.16$	$1 + h/R$;		
γ	angle between nadir vector and direction of scattering element;		
$\gamma_a 1.25 \times 10^{-2}$ rad	angular extent of antenna gain;		
ζ	angle between $\hat{\mathbf{n}}_r$ and $\hat{\mathbf{n}}_v$ (see Fig. 3);		
$\zeta_b 2 \times 10^{-4}$ rad	angular extent of along-track beam;		
ξ_b	look-angle of along-track beam;		
ξ_{mb}	see (23) and Fig. 4;		
ξ_i	polar coordinate of the baseline vector;		
σ^0	surface backscattering coefficient;		
σ_s	standard deviation of surface roughness;		
σ_v	volume backscatter coefficient;		

APPENDIX B

STATISTICS OF THE MULTILOOKED ECHO

The single-look echo power $_{st}\Omega^{(1)}$ is exponentially distributed with mean $_{st}P_r^{(1)}$. In consequence, with the coefficient μ defined to be

$$\mu = \frac{\left(_{ml}P_r^{(1)}\right)^2}{\sum_k \left(_{st}P_r^{(1)}\right)^2} N \quad (\text{B1})$$

the variance of the multilooked power is that given by (43).

The statistics of the multilooked cross product $_{ml}\Xi^{(1,2)}$, and the phase derived from it, are generally complicated. However,

if the number of looks is large and the coherence reasonably high, the situation is greatly simplified, and that is the case we treat here. Firstly, while allowing that the mean echo varies from look to look, we suppose that the mean phase does not. (Fig. 9 shows this to be a good assumption in practice.) It is then convenient to consider (without loss) the statistics of $ml\Xi^{(1,2)}e^{-i\text{Arg}[E\{ml\Xi^{(1,2)}\}]}$, whose mean is a real quantity. Then, if the number of looks is large, the fluctuations of the multilooked cross product about its mean will be small. In addition, provided the coherence is high, the real part of the multilooked cross product $ml\Xi^{(1,2)}e^{-i\text{Arg}[E\{ml\Xi^{(1,2)}\}]}$ will greatly exceed its imaginary part. In this case

$$\begin{aligned} & \text{Arg} \left(ml\Xi^{(1,2)}e^{-i\text{Arg}[E\{ml\Xi^{(1,2)}\}]} \right) \\ & \sim \frac{\text{Im} \left(ml\Xi^{(1,2)}e^{-i\text{Arg}[E\{ml\Xi^{(1,2)}\}]} \right)}{E \left\{ ml\Xi^{(1,2)}e^{-i\text{Arg}[E\{ml\Xi^{(1,2)}\}]} \right\}} \\ & = \frac{\text{Im} \left(ml\Xi^{(1,2)}e^{-i\text{Arg}[E\{ml\Xi^{(1,2)}\}]} \right)}{\frac{1}{N} \sum_k |sl\Psi^{(1,2)}|} \end{aligned} \quad (\text{B2})$$

and the statistics of the phase are determined by those of the imaginary component.

The single-look cross product $ml\Xi^{(1,2)}e^{-i\text{Arg}[E\{ml\Xi^{(1,2)}\}]}$ has a distribution function given in [14]. Its imaginary component has zero mean and a variance given by $\left((slPr^{(1)})^2 - |sl\Psi^{(1,2)}|^2 \right) / 2$. In consequence, the variance deviation of the multilooked phase is, approximately

$$\begin{aligned} & E \left\{ \text{Arg}^2 \left[ml\Xi^{(1,2)}e^{-i\text{Arg}[E\{ml\Xi^{(1,2)}\}]} \right] \right\} \\ & = \frac{\sum_k \left((slPr^{(1)})^2 - |sl\Psi^{(1,2)}|^2 \right)}{\left(\sum_k |sl\Psi^{(1,2)}| \right)^2}. \end{aligned} \quad (\text{B3})$$

If one then defines the multilooked coherence function $mlK^{(1,2)}$ to be

$$slK^{(1,2)} = \left(1 + \mu N \frac{\sum_k \left((slPr^{(1)})^2 - |sl\Psi^{(1,2)}|^2 \right)}{\left(\sum_k |sl\Psi^{(1,2)}| \right)^2} \right)^{-1/2} \quad (\text{B4})$$

one obtains (44).

More exact calculations would appear to demand Monte Carlo techniques. However, in the case that the power and coherence are independent of look angle (which is not the case considered in this paper), the density function of the multilooked cross product is known analytically [14]. In this case, the formula (B4) is good to 5% for all values of $K^{(1,2)} > 0.8$

and $N > 30$. Considering that these formulas are used to estimate the measurement error, this seems perfectly adequate.

REFERENCES

- [1] H. J. Zwally, "Growth of greenland ice sheet: Measurement," *Science*, vol. 246, pp. 1587–1589, 1989.
- [2] D. J. Wingham, A. J. Ridout, R. Sharroo, R. J. Arthern, and C. K. Shum, "Antarctic elevation change 1992 to 1996," *Science*, vol. 282, pp. 456–458, 1998.
- [3] J. L. Bamber, D. G. Vaughan, and I. Joughin, "Widespread complex flow in the interior of the Arctic ice sheet," *Science*, vol. 287, pp. 1249–1250, 2000.
- [4] A. Shepherd, D. J. Wingham, J. A. D. Mansley, and H. F. J. Corr, "Inland thinning of Pine Island Glacier, West Antarctica," *Science*, vol. 291, pp. 862–864, 2001.
- [5] N. R. Peacock and S. W. Laxon, "Sea surface height determination in the Arctic Ocean from ERS altimetry," *J. Geophys. Res.*, vol. 109, no. C7, 2004. DOI: 10.1029/2001JC001026.
- [6] S. W. Laxon, N. R. Peacock, and D. Smith, "Inter-annual variability in Arctic sea ice thickness," *Nature*, to be published.
- [7] J. T. McGoogan, "Satellite altimetry applications," *IEEE Trans. Microwave Theory Tech.*, vol. MTT-233, pp. 970–978, 1975.
- [8] H. J. Zwally, B. Schutz, W. Abdulati, J. Abshire, C. Bentley, A. Brenner, J. Bufton, J. Dezio, D. Hancock, D. Harding, T. Herring, B. Minster, K. Quinn, S. Palm, J. Spinhrine, and R. Thomas, "ICESat's laser measurements of polar ice, atmosphere, ocean and land," *J. Geodyn.*, vol. 34, pp. 405–445, 2002.
- [9] D. Wingham. (1999) CryoSat science and mission requirements. Dept. Space and Climate Physics, Univ. College London, CPOM. [Online]. Available: <http://www.esa.int/export/esaLP/cryosat.html>.
- [10] Y.-H. Kim, "Multimode-Scanning-Radar-Altimeter (MSRA) with synthetic aperture," in *Proc. ESA Consultative Meeting on Imaging Altimeter Requirements Techniques*, C. G. Rapley, H. D. Griffiths, and P. A. M. Berry, Eds., Dorking, U.K., May 30–June 1 1990.
- [11] M. Wolf and D. J. Wingham, "The status of the world's public-domain digital topography of the land and ice," *Geophys. Res. Lett.*, vol. 19, pp. 2325–2328, 1992.
- [12] B. Rabus, M. Eineder, A. Roth, and R. Bamler, "The shuttle radar topography mission—A new class of digital elevation models acquired by spaceborne radar," *ISPRS J. Photogramm. Remote Sens.*, vol. 57, pp. 241–262, 2003.
- [13] R. K. Raney, "The delay Doppler radar altimeter," *IEEE Trans. Geosci. Remote Sensing*, vol. 36, pp. 1578–1588, Sept. 1998.
- [14] J. R. Jensen, "Angle measurement with a phase monopulse radar altimeter," *IEEE Trans. Antennas Propagat.*, vol. 47, pp. 715–724, Apr. 1999.
- [15] L. Phalippou, P. Piau, D. J. Wingham, and C. Mavrocordatos, "High resolution radar altimeter for ocean and ice sheet monitoring," in *Proc. IGARSS*, Seattle, WA, July 1998, pp. 2020–2022.
- [16] C. R. Francis, "CryoSat Mission and data description," ESTEC, Noordwijk, The Netherlands, Doc. CS-RP-ESA-SY-0059, 2001.
- [17] D. J. Wingham, "A method for determining the average height of a large topographic ice sheet from observations of the echo received by a satellite altimeter," *J. Glaciol.*, vol. 41, pp. 125–141, 1995.
- [18] R. J. Arthern and D. J. Wingham, "Controls on ERS altimeter measurements over ice sheets: Footprint scale topography, backscatter fluctuations, and the dependence of microwave penetration depth on satellite orientation," *J. Geophys. Res.*, vol. 106, pp. 33 471–33 484, 2001.
- [19] D. J. Wingham, "The limiting resolution of ice sheet elevations derived from pulse-limited satellite altimetry," *J. Glaciol.*, vol. 41, pp. 413–422, 1995.
- [20] G. S. Brown, "The average impulse response of a rough surface and its implications," *IEEE Antennas Propagat.*, vol. AP-25, pp. 67–74, Jan. 1977.
- [21] J. R. Jensen, "Radar altimeter gate tracking: Theory and extension," *IEEE Trans. Geosci. Remote Sensing*, vol. 37, pp. 651–658, Mar. 1999.



D. J. Wingham received the B.Sc. degree from the University of Leeds, Leeds, U.K., in 1979, and the Ph.D. degree from the University of Bath, Bath, U.K., in 1984, both in physics.

He joined University College London in 1986, where he held lecturing posts at the Mullard Space Science Laboratory and the Department of Electronic and Electrical Engineering. He was appointed to a Chair in the Department of Space and Climate Physics in 1996. He is currently the Director of the Natural Environment Research Council (NERC)

Centre for Polar Observation and Modeling and is a member of the NERC Science and Technology Board and Earth Observation Experts Group. He is also Lead Investigator of the ESA CryoSat satellite mission.



Laurent Phalippou received the Master's degree in microwave electronics from University Paul Sabatier, Toulouse, France, in 1987, and the Ph.D. degree in signal and image processing from Ecole Nationale Supérieure des Télécommunications, Paris, France, in 1991.

He joined Alcatel Space in 1987, focusing on microwave passive radiometry and SAR processing. In 1991, he joined the European Centre for Medium-range Weather Forecast, Reading, U.K., as a Research Scientist, where his work focused

on radiative transfer modeling and variational assimilation of microwave radiometer radiances (SSM/I). In 1996, he returned to Alcatel Space and was responsible for the early definition of SIRAL and its performances during the B/C/D phases. He is currently Program Manager of the Poseidon-3 altimeter of the Jason-2 mission and the Responsible of the Alcatel Space altimeter product line.



C. Mavrocordatos received the Diplome d'Ingenieur Electronicien degree in electronics engineering from the Institute of Industrial Chemistry and Physics, Lyon, France, in 1984, and the Ph.D. degree in electronics from Sup' Aero, Toulouse, France, in 1990.

He joined Alcatel Space in 199, where he was responsible for radar instrument studies and developments. He was in charge of the development of Poseidon-2 altimeter (currently flying on Jason satellite mission) in Phase B, when he joined the European

Space Agency (ESA) in 1995. He is currently the Payload Manager of the ESA CryoSat mission and is in charge of the SIRAL instrument (SAR/Interferometric Radar Altimeter).



D. Wallis received the Diplome d'Ingenieur Electronicien degree from De Montfort University, Leicester, U.K., in 1997, and the Ph.D. degree from the University of Kent, Canterbury, U.K., in 2000, both in physics.

He was awarded a two-year fellowship by the Open University, where he studied the morphology of lunar and Martian impact craters using measurements made by satellite altimeters. He is currently a Research Fellow with University College London, working on the ESA CryoSat mission.